

The Journal of Physiology

<https://jp.msubmit.net>

JP-RP-2023-283728R2

Title: Adaptive spike threshold dynamics associated with sparse spiking of hilar mossy cells are captured by a simple model

Authors: Anh-Tuan Trinh
Mauricio Girardi-Schappo
Jean-Claude Béïque
Andre Longtin
Leonard Maler

Author Conflict: No competing interests declared

Author Contribution: Anh-Tuan Trinh: Conception or design of the work; Acquisition, analysis or interpretation of data for the work; Drafting the work or revising it critically for important intellectual content; Final approval of the version to be published; Agreement to be accountable for all aspects of the work Mauricio Girardi-Schappo: Acquisition, analysis or interpretation of data for the work; Drafting the work or revising it critically for important intellectual content; Final approval of the version to be published; Agreement to be accountable for all aspects of the work Jean-Claude Béïque: Conception or design of the work; Drafting the work or revising it critically for important intellectual content; Final approval of the version to be published; Agreement to be accountable for all aspects of the work Andre Longtin: Conception or design of the work; Drafting the work

Disclaimer: This is a confidential document.

or revising it critically for important intellectual content; Final approval of the version to be published; Agreement to be accountable for all aspects of the work Leonard Maler: Conception or design of the work; Drafting the work or revising it critically for important intellectual content; Final approval of the version to be published; Agreement to be accountable for all aspects of the work

Running Title: Hilar mossy cells exhibit adaptive spike threshold dynamics

Dual Publication: No

Funding: Canadian Institutes for Health Research: Jean-Claude Béïque, Andre Longtin, Leonard Maler, 153143; Brockhouse Award Fund: Andre Longtin, Leonard Maler, 493076-2017; Gouvernement du Canada | Natural Sciences and Engineering Research Council of Canada (NSERC): Andre Longtin, RGPIN/06204-2014; Krembil Foundation: Jean-Claude Béïque, Andre Longtin, Leonard Maler, N/A

Title: Adaptive spike threshold dynamics associated with sparse spiking of hilar mossy cells are captured by a simple model

Abbreviated title: Hilar mossy cells exhibit adaptive spike threshold dynamics

Anh-Tuan Trinh^{1,2*}, Mauricio Girardi-Schappo^{3,4*}, Jean-Claude Béïque^{2,5,6}, André Longtin^{4,5,6}, Leonard Maler^{2,5,6}

1. *Current address:* Kavli Institute for Systems Neuroscience, Norwegian University of Science and Technology, Trondheim, Norway, 7030

2. Department of Cellular and Molecular Medicine, University of Ottawa, Ottawa, Ontario, Canada, K1H 8M5

3. *Current address:* Departamento de Física, Universidade Federal de Santa Catarina, 88040-900, Florianópolis, Santa Catarina, Brazil.

4. Department of Physics, University of Ottawa, Ottawa, Ontario, Canada, K1N 6N5

5. Brain and Mind Institute, Center for Neural Dynamics, University of Ottawa, Ottawa, Ontario, Canada, K1H 8M5

6. Center for Neural Dynamics, University of Ottawa, Ottawa, Ontario, Canada, K1H 8M5

*These authors (A-T. T & M. G-S) contributed equally to this manuscript.

Corresponding author:

Anh-Tuan Trinh

Email: anh.t.trinh@ntnu.no

Number of pages: 46

Number of tables: 2

Number of figures: 8

Number of words for Abstract: 236

This manuscript was first published as a preprint: Trinh, A. T., Girardi-Schappo, M., Béïque, J. C., Longtin, A., & Maler, L. (2022). Dentate gyrus mossy cells exhibit sparse coding via adaptive spike threshold dynamics. *bioRxiv*. <https://doi.org/10.1101/2022.03.07.483263>

Key point summary

- Previous studies have shown that hilar mossy cells (hMCs) are implicated in pattern separation and the formation of spatial memory, but how their intrinsic properties relate to their *in vivo* spiking patterns is still unknown.
- Here we show that the hMC displayed electrophysiological properties that distinguishes them from the other hilar cell types including a highly adaptive spike threshold that decays slowly.
- The spike-dependent increase in threshold combined with an after-hyperpolarizing potential mediated by a slow K^+ conductance are hypothesized to be responsible for the low-firing rate of the hMC observed *in vivo*.
- The hMC's features are well captured by a modified stochastic exponential integrate-and-fire model that has the unique feature of a threshold intrinsically dependant on both the stimulus intensity and the spiking history.
- This computational model will allow future work to study how the hMCs can contribute to spatial memory formation and navigation.

Abstract

Hilar mossy cells (hMCs) in the dentate gyrus (DG) receive inputs from DG granule cells (GCs), CA3 pyramidal cells and inhibitory interneurons, and provide feedback input to GCs. Behavioural and *in vivo* recording experiments implicate hMCs in pattern separation, navigation and spatial learning. Our experiments link hMC intrinsic excitability to their synaptically evoked *in vivo* spiking outputs. We performed electrophysiological recordings from DG neurons and found that hMCs displayed an adaptive spike threshold that increased both in proportion to the intensity of injected currents, and in response to spiking itself, returning to baseline over a long timescale, thereby instantaneously limiting their firing rate responses. The hMC activity is additionally limited by a prominent medium after-hyperpolarizing potential (AHP) generated by small conductance K^+ channels. We hypothesize that these intrinsic hMC properties are responsible for their low *in vivo* firing rates. Our findings extend previous studies that compare hMCs, CA3 pyramidal cells and hilar inhibitory cells and provide novel quantitative data that contrasts the intrinsic properties of these cell types. We developed a phenomenological exponential integrate-and-fire model that closely reproduces the hMC adaptive threshold nonlinearities with respect to their threshold dependence on input current intensity, evoked spike latency and long-lasting spike-induced increase in spike threshold. Our robust and computationally efficient model is amenable to incorporation into large network models of the DG that will deepen our understanding of the neural bases of pattern separation, spatial navigation, and learning.

Introduction

The dentate gyrus (DG) has long been discussed in relation to its putative roles in pattern separation and the generation of spatial maps (Marr, 1971; Leutgeb *et al.*, 2007; Yassa & Stark, 2011; Neunuebel & Knierim, 2014). Given their large numbers, sparse activity and connectivity features (Diamantaki *et al.*, 2016), DG granule cells (GCs) have been associated with pattern separation of their entorhinal cortex (EC) inputs (McNaughton & Morris, 1987; Rolls *et al.*, 1998; Yassa *et al.*, 2011). A subset of GCs is endowed with single place fields (GoodSmith *et al.*, 2017), directly implying a role in spatial location encoding. These studies have rarely considered the excitatory hilar mossy cells (hMC) which receive GC input and then feedback to GCs (Scharfman, 1994b, 2016). Recent studies have begun to directly implicate hMCs in both pattern separation (Jinde *et al.*, 2012; Bui *et al.*, 2018) and the encoding of spatial location (Danielson *et al.*, 2017; GoodSmith *et al.*, 2017; Senzai & Buzsaki, 2017). However, unlike the GCs, single hMCs can discharge at multiple locations in space, thereby encoding multiple place fields (GoodSmith *et al.*, 2017) and highlighting the singular properties of this feedback pathway. Remarkably, neurons displaying connectivity (Elliott *et al.*, 2017) and functional features (Fotowat *et al.*, 2019) analogous to those of hMCs were recently described in a teleost analogue of the hippocampal network, suggesting that hMC circuitry subserves a conserved role in the encoding of spatial maps.

The hMCs receive synaptic input from CA3 pyramidal cells as well as from GCs and the dynamic properties of these inputs onto hMCs have been studied (Scharfman *et al.*, 1990; Scharfman, 1991, 1994b). The hMC feedback projections to GCs are both direct (excitatory) and via inhibitory interneurons (Scharfman, 1995) and the dynamic properties of these synapses have also been investigated (Hashimotodani *et al.*, 2017; Hedrick *et al.*, 2017; Lituma *et al.*, 2021). These connectivity and physiology features suggest that hMCs act as a comparator of GC and CA3 activities (Elliott *et al.*, 2017) regulating the activity of the GC population via feedback. However, there is limited knowledge about the intrinsic biophysical properties of hMCs (Scharfman, 1992; Buckmaster *et al.*, 1993; Scharfman, 1993; Buckmaster & Schwartzkroin, 1995), which would be essential to understand the putative “comparator” role emerging from its synaptic inputs. For example, *in vivo* recordings of hMCs have revealed that they often spike in a complex patterned manner (GoodSmith *et al.*, 2017; Senzai & Buzsaki, 2017), but it is

unknown whether their spike output is simply a reflection of their dynamic synaptic inputs or whether intrinsic hMC dynamics also contribute to the patterning.

Here, we present a combined electrophysiological and computational analysis that identified salient features of intrinsic properties of hMCs, notably spike frequency adaptation mechanisms with a special emphasis on dynamic spike threshold. We compared the dynamic spike threshold across major cell types in the hippocampus: GCs, CA3 pyramidal cells, hilar inhibitory interneurons and CA1 pyramidal cells to reveal the dynamics of hMCs, shedding light on the function of these “enigmatic” cells (Scharfman, 2016). In particular, we extend the analysis of Buckmaster et al (1993) to emphasize similarities as well as differences in the physiology of hMCs and CA3 pyramidal cells.

The main features of this electrophysiological characterization were used to develop and validate a lightweight (in the sense of mathematically concise and computationally efficient) phenomenological exponential integrate-and-fire (EIF) model of hMC dynamics. Our model accounts for spiking memory through threshold adaptation and is particularly novel in its intricate dynamical dependencies on input properties that are specific to the hMCs (some of which are counter-intuitive). Its format favours its inclusion in large-scale DG network models to gain insights into how they might integrate GC and CA3 pyramidal cell inputs to generate the spike patterns and place fields observed *in vivo*.

Materials and Methods

Ethical approval

All animal procedures were approved by the University of Ottawa Animal Care and Veterinary Service (Protocol#: CMM-3017). The facility is registered under the *Animal for Research Act* and follow the guidelines established by the Canadian Council on Animal Care. All effort was made to minimize the number of animals used and animal suffering.

Animals

For this study, we used 26-55 day old mice from the following transgenic mouse lines for cell type-specific identification; PV:TdTomato was obtained from crossing the PV-cre mouse line (B6.Cg-Pvalbtm4.1(flop)Hze/J; Jackson Labs; RRID:IMSR_JAX:022730) with the Rosa:TdTomato (B6.Tg-Gt(ROSA)26Sortm14(CAG-tdTomato)Hze/J; Jackson Labs; RRID:IMSR_JAX:007914) and the SOM:TdTomato was obtained from crossing the

aforementioned RosaTdTomo mice with the SOM-cre (Sst-IRES-Cre; Jackson Labs; RRID:IMSR_JAX:013044) mice. These mice were used to obtain recordings from hilar parvalbumin (PV, N = 8 slices from 7 animals) and hilar somatostatin (SOM, N = 8 slices from 7 animals) inhibitory interneurons respectively. The hMC recordings were obtained from Drd2:TdTomo mice. The Drd2-cre (B6.FVB(Cg)Tg(Drd2-cre)ER44Gsat/Mmucd, RRID:MMRRC_032108-UCD) was crossed with the Rosa:TdTomo mouse line (N = 34 slices from 30 animals). For the other readily identifiable excitatory cell types (DG granule cells, CA3 pyramidal neurons and CA1 pyramidal neurons), recordings were obtained in wild type animals (C57BL/6 mice) (DG granule cells: N = 9 slices from 9 animals, CA3: N = 8 slices from 8 animals; CA1: N = 6 slices from 5 animals). Animals were maintained in a normal light/dark (12h-12h) cycle in a temperature-controlled room (~22°C) and had access to food and water *ad libitum*. Animals from both sexes were used for this study. No sex differences were observed in the biophysical properties of the hippocampal cells studied and data from male and female mice was therefore pooled. Rodents in this age range are capable of learning and our conclusions and model will therefore be applicable to studies of pattern separation and spatial learning in mice (Langston *et al.*, 2010; Wills *et al.*, 2010).

***In vitro* slice procedure**

Early experiments instructed us that we could reliably obtain quality recordings from hMCs neurons in slices prepared from young mice (<30 days old) using a slicing procedure routinely used for mice hippocampal recordings (Lee *et al.*, 2016). However, hMCs in slices from older animals proved to be highly vulnerable and were not amenable to stable and long-lasting electrophysiological recordings. We therefore iteratively developed a slicing procedure to maximize hMC health for recordings in older animals. Prior to the dissection, an N-methyl-D-glucamine (NMDG) cutting solution and a modified recovery Ringer solution were placed in two distinct slice chambers. The NMDG solution was adapted from Ting *et al.* (2014), and contained (in mM): 92 NMDG, 2.5 KCl, 1.25 NaH₂PO₄, 30 NaHCO₃, 20 HEPES, 10 MgSO₄, 25 Glucose, 0.5 CaCl₂·2H₂O, 5 Ascorbic Acid, 2 Thiourea, 10 N-acetyl-L-cysteine, 3 Sodium Pyruvate, and was adjusted to 295 mOsm while the modified recovery ACSF solution contained (in mM): 92 NaCl, 2.5 KCl, 1.25 NaH₂PO₄, 30 NaHCO₃, 2 MgSO₄, 25 Glucose, 2 CaCl₂, 5 Ascorbic Acid, 2 Thiourea, 10 N-acetyl-L-cysteine, 3 Sodium Pyruvate, and was adjusted to 295 mOsm. Both recovery chambers were oxygenated (95% O₂, 5% CO₂) and heated to 37°C.

At the same time, another beaker containing the NMDG cutting solution (roughly 350 mL) was oxygenated and chilled to 4°C. Once the NMDG cutting solution was ready, the mouse was anesthetized by isoflurane inhalation (4% isoflurane, Baxter Corporation, Canada). A transcardiac perfusion (10 mL) was then performed in order to exchange the animal's blood with 3 mL of the chilled NMDG cutting solution after which the animal was euthanized by decapitation. Once the brain was removed and placed in the chilled cutting solution, coronal sections (300 µm thick) were obtained using a vibratome (Leica Biosystems) and the slices were transferred to the previously heated (to 37°C) custom-made incubation chamber containing the NMDG cutting solution. Before the slices were transferred to the heated NMDG cutting solution, both incubation chambers (one containing the NMDG cutting solution and the other, the recovery artificial cerebrospinal fluid, ACSF) were removed from the heating bath and were left to rest at room temperature. After 7-10 minutes, the coronal slices were transferred to the other incubation chamber containing the recovery Ringer (ACSF) solution for at least 45 mins until the time of recording.

***In vitro* recordings**

Whole-cell recordings were carried out in recording ACSF (119 mM NaCl, 26 mM NaHCO₃, 11 mM glucose, 2.5 mM KCl, 1 mM NaH₂HPO₄-H₂O, 2.5 mM CaCl₂, 1.35 mM MgSO₄, and 295 mOsm, pH 7.4) in a perfused recording chamber at room temperature (23-25°C). Given the small size of the hMCs compared to the CA3/CA1 pyramidal neurons, borosilicate glass micropipettes (Sutter Instruments) with resistances ranging between 5-12 MΩ, filled with a K-gluconate-based intracellular solution (135 mM K-gluconate, 7 mM KCl, 10 mM HEPES, 4 mM Mg-ATP, 10 mM phosphocreatine, and 0.4 mM Na-GTP, with an osmolality of 295 mOsm, pH 7.2), were used for recordings. Neurons were visualized with differential interference contrast (DIC) optics using a CMOS infrared camera (Scientifica). The recordings were first amplified using a Multiclamp 700B (Molecular Devices), filtered at 3 kHz and sampled at 10 kHz using a Digidata 1550 (Molecular Devices). All recordings were carried out in pCLAMP 10 (Molecular Devices, RRID:SCR_011323) and in current-clamp mode unless specified. At times, small DC current were applied to maintain the cell hyperpolarized at around -75mV. After attaining the whole-cell configuration, the resting membrane potential (RMP) was recorded for 30-60 s after which 500 ms square pulse currents of varying magnitude were injected into the cell. To characterize the slowly adapting spike threshold we encountered (see Results), we administered

a ramp current injection protocol as previously described in (Trinh *et al.*, 2019). Recorded cells were held for roughly 20-45 minutes, depending on the health of the cell. We generally limited current injection to a maximum of 200 pA to assure the stable long-term health of the recorded cells. In the case of hMCs, we extended this current range to 300 pA in order to capture the full nonlinear response of these cells in our model (Fig. 4A, inset).

Pharmacology

During this study, we used a glutamatergic receptor antagonist (10 μ M cyanquixaline, or CNQX, Millipore-Sigma, Cat No. C239) and a GABA_A chloride channel blocker (0.1 mM picrotoxin, or PTX, Abcam, Cat No. ab120315) to abolish synaptic activity during our recordings. To quantify the contribution of spiking to the spontaneous membrane noise, we have bath applied 0.5 μ M tetrodotoxin (TTX, Abcam, Cat No. ab120054), a Na⁺ channel antagonist (Alle & Geiger, 2006). Furthermore, we also used a Ca²⁺-activated slow conductance K⁺ (SK) channel blocker, 30 μ M UCL1684 (Tocris, Cat. No. 1310) to study the after-hyperpolarizing potential (AHP) in hMCs.

Data analysis

Recordings were first visualized in Clampfit (Molecular devices) and then subsequently analysed in MATLAB[®] 2020a (MathWorks[®], RRID:SCR_001622) using custom scripts. To identify postsynaptic potential events in current-clamp, we developed a threshold-based method where the first derivative of the RMP was first smoothed with a moving average filter. Afterwards, an arbitrary threshold (0.05 mV·ms) was used to detect the peak of each event. The amplitude was calculated by subtracting the peak of each event with the baseline prior to each event. Given that this was a crude method for detecting events, we did not differentiate between individual and summed events which may have caused us to underestimate the true number of postsynaptic events. For recordings in voltage-clamp, the events were first identified using template matching in Clampfit and then subsequently analysed in MATLAB. For the passive properties defined in Table 1, the resting membrane potential (RMP) was calculated prior to the injection of any DC holding current. The input resistance of a cell was calculated using the slope of the I-V curve that was obtained from depolarizing current injections in current-clamp mode. The membrane time constant was measured by fitting an exponential function to the cell's response following a hyperpolarizing current injection. The spike amplitude was defined as the distance between the spike height and the average resting membrane potential prior to the

depolarizing current injection. The spike half-width was defined as the midway point between the spike threshold and the maximal height of the spike. The spike threshold was defined as the value corresponding to an arbitrary chosen fraction (0.033) of the peak of the 1st derivative of the membrane potential (Azouz & Gray, 2000; Trinh *et al.*, 2019). This method has been shown to provide an accurate estimate of spike threshold when compared to other similar methods (Sekerli *et al.*, 2004). The difference in spike threshold (hereafter called *delta spike threshold*) was defined as the difference between the first and nth spike threshold. The latency to 1st spike was measured as the time from the onset of the intracellular current injection to the peak of the 1st evoked spike. Here we defined the AHP as the hyperpolarizing potential that typically occurs following an action potential. Since the AHP changes over time because of the dynamic spike threshold, we sought to compensate for this by calculating the AHP maximum amplitude as the difference between the spike threshold of the prior spike (spike “n”, or the 1st evoked spike) and the minimum recorded voltage during the inter-spike interval (ISI) between spike “n” and spike “n+1”, *i.e.*, at the AHP trough. We estimated the total amplitude of the medium AHP area as the area of the AHP between its trough and extending to the membrane potential equal to the spike threshold of the previous spike (Fig. 3B, inset).

A model for the Hilar Mossy Cell dynamics

We were interested in finding a minimal model that can capture the key features of the hMC responses to inputs, with emphasis foremost on the spike threshold increase and decay following spiking. Our purpose is to provide an augmented integrate-and-fire-like dynamics whose few parameters can be readily fitted to data, and which can readily be incorporated into modern brain simulation tools such as BRIAN and NEST (Gewaltig & Diesmann, 2007; Stimberg *et al.*, 2019). It will consequently enrich large-scale dynamical models of hippocampus by implementing realistic hMC dynamics. Given the lack of detailed knowledge of the kinetics of all channels expressed by hMCs (see below), we opted for a reduced model with some biophysically accessible parameters. This is in contrast to using a Hodgkin-Huxley-type model that pieces together the kinetics of different channels from other models, since such detailed model would involve dozens of estimated parameters and would be computationally expensive to run in network settings.

Specifically, we investigated the standard leaky integrate-and-fire (LIF) and the exponential integrate-and-fire (EIF) models and found that the latter could be suitably expanded and subsequently fitted to reproduce the data. We did this process iteratively: we added a feature, then simulated the improved model and compared the following features with experiments: spike-dependent threshold increase, input-dependent threshold of the first spike, spike threshold decay, AHP effect (the dependence of the minimum of the AHP on the spike threshold), and the latency to the first spike. A simple minimal model able to capture these five features is given by:

$$\begin{aligned}
\tau \frac{dV}{dt} &= V_b - V + ke^{\frac{V-\theta(t)}{k}} + RI_{ext} + \frac{\sigma}{2} \tau \eta(t) , \\
\tau_1 \frac{d\theta}{dt} &= V_0 + sf(R_\theta(I_{ext} - I_0)) - \theta , \\
\tau_\theta \frac{d\theta_s}{dt} &= -\theta_s ,
\end{aligned} \tag{1}$$

where V is the membrane potential and $f(V) = V/(1 + |V|)$ is a logistic function. The total threshold is dynamic and computed as the sum of two components (see below) as $\theta(t) = \theta(t) + \theta_s(t)$; The time-dependent process $\eta(t)$ is a Gaussian white noise with zero mean and unit standard deviation. It is added in order to mimic the statistical variability of the observed hMC behaviour, making the model generic and robust to small parameter variations. All the parameters are given in Table 2.

In the standard EIF model, a spike occurs when the voltage runs off to infinity; a numerical criterion is then used to detect this upswing, followed by a manual resetting of the voltage. Accordingly, whenever $V(t) > V_{peak}$, a >60 mV spike is said to have occurred. The voltage and the spike-dependent part of the threshold are then reset in the subsequent time step according to:

$$\begin{aligned}
V(t + dt) &= V_b + \alpha(V(t) - V_b) - \delta , \\
\theta_s(t + dt) &= \theta_s(t) + \frac{V_m - \theta_s(t)}{V_m} \Delta\theta .
\end{aligned} \tag{2}$$

We did not need to include an absolute refractory period given the low firing rates and a mean action potential width of 5 ms; the resetting of the voltage and threshold following a spike effectively mimics a refractory effect. We solve these equations using a second-order stochastic Runge-Kutta method (Honeycutt, 1992).

It is worth noticing that we only fixed the most basic membrane parameters to the observed features in hMCs, and then used the other parameters to obtain good fits to the hMC data. The

fixed parameters are the average resting membrane potential, the noise amplitude, the reset voltage slope (covariation of AHPs with threshold), the membrane time constant, and the threshold baseline (no hMC was observed emitting a spike with threshold smaller than this value). The reason for our choice is that we are proposing a model for a generic hMC, and hence the parameters must be able to vary within a reasonable range. Furthermore, we checked the robustness of our model against changes in the parameters.

The exponential term in the voltage dynamics describes the rise of the spike more naturally as compared to a simple LIF (Fourcaud-Trocmé *et al.*, 2003), *i.e.*, it mimics the positive feedback between voltage and sodium channel activation. Here, we replaced the standard EIF parameter for spike threshold V_T by a dynamic variable, $\theta(t)$. This variable is composed of two terms: the input-dependent part, $\theta(t)$, is directly derived from experimental observations; *it is counter-intuitive* in that it increases as the external input increases, as observed in our data. It works similarly to an input-dependent activation gating variable, since the function $f(V)$ is a sigmoid and plays the role of an activation function. We chose the logistic function instead of a Boltzmann function because of its numerical efficiency (Girardi-Schappo *et al.*, 2017). The spike-dependent term $\theta_s(t)$ in the total threshold saturates at V_m as described in Eq (2). This term was introduced to enhance the fitting to the spike-dependent experimental data of hMCs, and it receives a discontinuous kick proportional to $\Delta\theta$ at every spike (Benda et al., 2010). After each spike, the spike-dependent threshold θ_s recovers exponentially with time constant τ_θ . This also causes a net recovery to the total threshold $\theta(t)$ of the model, matching the observed hMC behavior.

In the absence of noise and a step input, the model has a stable fixed point, corresponding to the resting membrane potential, as well as an unstable fixed point corresponding to a spike threshold. We measured the effective threshold of our EIF model by the same minimum derivative method described for the experiments. This is because the value of $\theta(t)$ does not represent an actual hard threshold for spiking, even though it depends on the unstable fixed point of the model. The nullcline (*i.e.*, the set of points where the time derivatives are zero) dynamically shifts when the cell is stimulated due to the feedback between $\theta(t)$ and the external input, such that the actual threshold becomes a function of time and has to be detected by the minimum derivative. In fact, the EIF model is known to present intrinsic threshold variability,

and here we are introducing a new mechanism that causes the threshold to covary with both the injected current and the firing of the cell.

The reset rule of the membrane potential is also different from the standard EIF dynamics in Eq. (2). We assume that, after the spike, the membrane potential is directly proportional (by a factor less than one) to the potential right before the spike – a feature that is present in many neurons (Teeter *et al.*, 2018). Here it is used specifically to implement a dependence of the AHP minimum on the spike threshold, compensating the post-spike threshold increase. Ultimately, this decreases the delay to the onset of the next spike, therefore increasing the evoked firing frequency when compared to a model with absolute reset and spike-dependent threshold.

Model simulation

We chose our model parameters so as to conform with the dependence of threshold and latency on input currents. In addition, we attempted to simulate the dynamic threshold of hMCs since this is likely an important regulator of the stimulus-evoked spike rates *in vivo*. We simulated the step and ramp injection experiments (described in the *In vitro* recordings and Results sections) to probe for the threshold increase and decay. As in the experimental data, the threshold of the model was calculated by taking a fraction of the peak (0.033 mV·ms) of the first derivative of the membrane potential. The AHP minimum was estimated by taking the minimum value of the membrane voltage in between two consecutive spikes for a given injected current.

For the step simulations, we considered a wider range of inputs than in the experiments, since we wanted to probe for the general behaviour of our modified EIF model. We considered currents from 70 pA to 400 pA. We ran 10 trials for each current and calculated the average and standard deviation for each spike threshold and for the latency to the first spike. The threshold increase as a function of the spike number was calculated by further averaging the threshold values of each spike over all the injected currents in the range of 70 pA to 350 pA, yielding an average input $\bar{I}_{ext} = 205$ pA.

The threshold decay was calculated from the two-ramp injection stimulation. We followed a protocol very similar to the one implemented experimentally (described in detail in the Results section). We first injected a stimulus ramp to excite the cell and cause the threshold to rise due to the spiking. Then, we injected a probe ramp after a certain delay to check the spike threshold at that later moment after the initial stimulation. We did 10 trials for each delay independently but kept the same maximum intensity and duration for both the stimulus (200 ms, 350 pA maximum)

and the probe (100 ms, 300 pA maximum) ramps. The average threshold and S.D. were calculated for each delay.

Code Accessibility

All codes related to the EIF model will be available upon request and they are also made available at the Github repository (<https://github.com/mgirardis/mossy-cell-dg>).

Statistical evaluation

Data points are presented as mean \pm standard deviation (SD). Where applicable, the statistical significance was determined using either the one-way ANOVA with the ad-hoc multiple comparison tests, the paired *t*-test, or the Kruskal-Wallis test with the associated multiple comparison test (Dunn's test) where $p < 0.05$ is considered significant (see statistical table). Statistical evaluations were performed using MATLAB[®] 2020a (MathWorks[®]).

Results

As previously reported (Buckmaster *et al.*, 1993; Scharfman, 1993), whole-cell electrophysiological recordings in current-clamp mode revealed that hMCs exhibit singularly large and frequent membrane potential fluctuations in the absence of any current injections (Fig. 1A). We present this data first in order to graphically illustrate that such fluctuations must be blocked in order to estimate both spike threshold and the AHP. Remarkably we found that, within the core hMC network, such fluctuations were confined to hMCs. These fluctuations were often greater than 10-20 mV and at times generated spontaneous spiking: average rate of 0.48 ± 0.21 Hz (maximal observed rate of 2.2 Hz) in a subset of our recordings where no holding current was used to artificially hyperpolarize the RM (inset Fig. 1A: N = 3 cells). If we also included cells that were hyperpolarized using a holding current (an additional 14 cells), then 9/17 hMC cells displayed spontaneous spiking. By only analysing cells without a holding current, we observed that these spontaneous spikes often occurred following the onset of large fluctuations, *i.e.*, >10 mV, suggesting that multiple smaller coincident fluctuations are required to evoke spontaneous spiking (Fig. 1B). Given that many of the recorded cells displayed spontaneous spiking, we opted to hold the hMCs at a hyperpolarized level compared to its average RMP (N = 14 cells, mean RMP: -64.6 ± 10.4 mV, Table 1) to prevent spontaneous spiking for future analyses (see Fig. 1G for an example of spontaneous spiking during current injection).

Previous studies have suggested that such fluctuations of the membrane potential may be caused by the stochastic opening and closing of various ion channels along the neuron's membrane, producing an approximately Gaussian distribution of the mean-subtracted membrane potential (Faisal *et al.*, 2008; Marcoux *et al.*, 2016). The mean-subtracted membrane potential distribution observed in hMCs was asymmetrical (Fig. 1C). This suggests that the membrane noise may not be intrinsic in nature but instead driven by synaptic input. Additionally, we quantified this difference by simply estimating the variance of the membrane potential and found that the hMC variance (N = 14 cells) was at least an order of magnitude greater than that of granule cells (N = 9 cells), CA1 (N = 7 cells) and CA3 pyramidal cells (N = 8 cells, Fig. 1D; one-way ANOVA: $p = 8.77 \times 10^{-9}$; multiple comparison test: GC vs CA3: $p = 1$; GC vs CA1: $p = 1$; CA1 vs CA3: $p = 1$; GC vs hMC: $p = 7.97 \times 10^{-7}$; CA3 vs hMC: $p = 2.13 \times 10^{-6}$; CA1 vs hMC: $p = 3.15 \times 10^{-6}$). Hilar inhibitory cells (PV: N = 8 cells, SOM: N = 9 cells) also had far less MP noise (Fig. 1D; multiple comparison test: PV vs SOM: $p = 0.88$; PV vs hMC: $p = 2.63 \times 10^{-6}$; SOM vs hMC: $p = 9.26 \times 10^{-5}$). This is in accordance with Buckmaster *et al.* (1993) who also noted that, in the rat, spontaneous MP fluctuations were more prominent in hMCs compared to CA3 pyramidal cells.

To test whether the observed noise is caused by spontaneous synaptic inputs, we bath applied the AMPA receptor antagonist CNQX (10 μ M; N = 14 cells; Fig. 1Ei). After this addition, the membrane potential variance dropped to negligible levels, from $10.7 \pm 6.9 \text{ mV}^2$ to $0.3 \pm 0.4 \text{ mV}^2$ (paired *t*-test; $p = 5.48 \times 10^{-5}$; Fig. 1Fi), demonstrating that these fluctuations were synaptically driven. Additionally, we quantified the contribution of GABA transmission membrane fluctuations by bath applying 0.1 mM picrotoxin (PTX), a GABA_A receptor antagonist (Fig. 1Eii). The addition of PTX resulted in only a non-significant reduction of the membrane potential fluctuations (N = 4; Control; $12.3 \pm 9.6 \text{ mV}^2$, PTX; $11.6 \pm 11.1 \text{ mV}^2$; paired *t*-test: $p = 0.61$; Fig. 1Fii) in accordance with a previous study (Scharfman, 1993). To further test whether the spontaneous events that we have observed were mostly driven by glutamatergic synapses, we have also performed (N = 2 cells) PTX wash-in experiments in voltage clamp while holding the membrane potential at -60 mV (Fig. 1G). When we examined the variance of these recordings, the mean variance did not change (Control: $168.0 \pm 71.9 \text{ pA}^2$, PTX: $174.4 \pm 159.2 \text{ pA}^2$) after the addition of PTX. Closer inspection of these RM traces prior to the addition of CNQX or PTX did not reveal any visually obvious hyperpolarizing potentials even when the slower depolarizing

events exceeded -70 mV (Fig. 1A). In order to more carefully assess this point, we injected depolarizing square pulse currents to increase the membrane potential above the reversal potential of Cl^- (i.e., >60 mV). However, the hMC's responses to these current injections still do not reveal any hyperpolarizing spontaneous potentials (Fig. 1H). These observations suggest that glutamatergic transmission was responsible for the substantial fluctuations of hMC membrane potential. Our results confirm earlier studies that have shown that the strong fluctuations of hMC membrane potential are due to spontaneously generated AMPA receptor mediated EPSPs. These studies have concluded that the likely source of these EPSPs is the DG granule cell mossy fibre projection to hMCs (Buckmaster *et al.*, 1993; Scharfman, 1993); hilar inhibitory cells also receive mossy fibre input (Acsady *et al.*, 1998) and it is therefore not clear why their MP noise is so much lower than that of hMCs.

The synaptic noise might be spike-driven or due to spontaneous release, that is, TTX-independent miniature EPSCs. To distinguish between these possibilities, we recorded hMC neurons in voltage-clamp and bath applied 0.5 μM of tetrodotoxin (TTX), a Na^+ channel antagonist, in order to prevent all spontaneous spiking activity ($N = 7$ cells; Fig. 2A, B). The bath application of TTX did not significantly affect the average spontaneous EPSC amplitude (Control: 49.2 ± 10.7 pA; TTX: 42.1 ± 7.3 pA; paired t test: $p = 0.06$, Fig. 2C). In contrast, the average frequency of spontaneous events fell from 10.9 ± 4.9 Hz to 6.1 ± 3.6 Hz after the application of TTX (paired t-test: $p = 0.0008$, Fig. 2D). This suggests that almost half of the spontaneous events were driven by spiking activity, presumably from neurons or severed axons within the slice. Moreover, the serial correlations of spontaneous events were near zero before and after the administration of TTX (Control: 0.04 ± 0.04 ; TTX: 0.04 ± 0.04 ; paired t-test; $p = 0.9$, Fig. 2E) strongly indicating that both the spontaneous and spike driven fluctuations were generated by renewal processes. Finally, when we plotted the histogram of interevent intervals, we also observed that the number of events was reduced after the addition of TTX (Fig. 2F) which further supports our findings that roughly half of the spontaneous events were driven by spiking within the hilar network. The interevent distributions of membrane fluctuation events were well fitted by exponential densities (decay time constant τ ; where Control: $\tau = 78.2 \pm 2.4$ ms, adjusted R-square: 0.999; TTX: $\tau = 123.8 \pm 6.0$ ms, adjusted R-square: 0.997) suggesting that the events were driven by Poisson processes. Given that a large number of spontaneous events were still present after the application of TTX, we hypothesize that these TTX-

independent events were caused by spontaneous release of synaptic vesicles. Potential sources of the spontaneous and spike driven noise are presented in the Discussion.

Hilar Mossy Cell Intrinsic Properties

To obtain a thorough characterisation of the hMCs for the computational model, we next focused on the intrinsic biophysical properties. The presence of synaptic noise greatly hindered the estimation of hMC spike threshold and quantification of hMC AHPs (Fig 1). These experiments were therefore carried out in the presence of a GABAergic antagonist (picrotoxin) 0.1mM PTX and a glutamatergic antagonist, 10 μ M CNQX, in order to achieve clean recordings suitable for such measurements. To examine the firing properties of these neurons, we injected square currents of various magnitudes. Remarkably, even strong current injection (+200 pA) hMCs did not induce high frequency spiking (average rate of 6.3 ± 3.6 Hz with +200 pA current injections, N = 14 cells: Fig. 3Ai, Aii). We thus decided to examine the mechanisms that contribute to this low intrinsic excitability of hMCs.

Previous studies have shown that the medium AHP (mAHP) is driven by Ca^{2+} -activated K^+ channels, *i.e.*, the small conductance K^+ (SK) channels (Kohler *et al.*, 1996; Engel *et al.*, 1999). Once the synaptic noise was removed by CNQX, we were able to visualize a prominent AHP which was previously masked by the barrage of PSPs (Fig. 3Aii, 2Bi). SK channels are expressed in neurons within the hilus of the rodent dentate gyrus (Cembrowski *et al.*, 2016). Bath application of the SK channel blocker UCL1684 (30 μ M) strongly affected the AHP (N = 6 cells; Fig. 3Bii) and induced a robust reduction in the area of the AHP (mean area for control: 156.0 ± 30.7 ; UCL1684: 61.6 ± 47.4 mV^2 , paired *t*-test; $p = 0.003$; Fig. 3C). The peak magnitude of the AHP was less affected by this antagonist although it was still significantly reduced (Fig. 3Bii; mean amplitude for control: 9.7 ± 2.3 mV; 6.1 ± 3.7 mV in UCL1684; paired *t*-test: $p = 0.018$; Fig. 3D). Thus, SK channels are a primary contributor of the mAHP in hMCs, but there may be other channels that contribute to the fastest component of the AHP in these cells.

Bath administration of UCL1684 also caused hMCs to spike at membrane potentials that were previously subthreshold (Fig. 3Bii), suggesting that SK channels may be active at subthreshold potentials and slightly delay the firing of the 1st spike. Previous studies have shown that SK channels are active at resting membrane potentials in mammalian neurons (Zhang & Huang, 2017). Furthermore, our previous study in the weakly electric fish (*Apteronotus*

leptorhynchus) has also revealed this to be the case in pallial neurons (Trinh *et al.*, 2019) but not in hindbrain electrosensory neurons (Ellis *et al.*, 2007). Consistent with both these papers, we found that the application of UCL1684 also caused the cell to fire more rapidly at first and then reach a more depolarized plateau potential (difference of ~ 9.2 mV between control and UCL1684 conditions; arrow in Fig. 3Bii). After the strong discharge, the hMCs cells stopped firing. We next examined the cellular basis of the strong spiking adaptation still present after the SK channel block.

Previous studies have shown that hilar mossy cells and hilar inhibitory interneurons are highly interconnected, and both receive inputs from neighbouring CA3 and DG granule cells (Amaral, 1978; Buckmaster & Schwartzkroin, 1994; Scharfman & Myers, 2012). We therefore compared intrinsic properties across these cell types because they could affect the reliability and temporal precision of the information transmitted by the hMCs within this network, notably the spike threshold and latency to 1st spike. For these analyses, we decided to compare the excitatory cells and the inhibitory cells separately since these classes of cells were shown to have similar within class spiking properties (Table 1). We have not injected currents larger than ~ 200 pA because most cells were not able to sustain spiking at higher current injections (>120 pA for GCs); further, we graph (Fig. 4, Suppl. Fig. 1A) but do not report the analyses for GCs because of the limited current range we could use for these cells. We observed that the excitatory hippocampal neurons displayed linear increases in spike threshold in response to rising current injections (see Fig. 4A for linear fit values). The increase was shallow for CA1 pyramidal cells so that, over 70 to 180 pA current range, their threshold only increased from -54.0 ± 3.2 to -50.0 ± 1.3 mV. In contrast, CA3 pyramidal neurons and hMCs displayed steeper slopes (Fig. 4Ai) and, over the same current range, their threshold increased from -47.8 ± 6.4 to -41.8 ± 5.5 mV and from -50.4 ± 7.4 to -41.0 ± 6.7 mV respectively. As such, CA3 and hMC neurons displayed a stimulus-dependent change in spike threshold that was significantly different to the CA1 pyramidal neurons (Kruskal-Wallis test: $p = 1.59 \times 10^{-4}$; multiple comparison test (Dunn's test): hMC vs CA3: $p = 0.99$; hMC vs CA1: $p = 0.015$; CA3 vs CA1: $p = 6.0 \times 10^{-4}$). Given our intention to model the hMC response to a wide range of synaptic currents, we stimulated them with currents up to 300 pA. As illustrated in Fig. 4Ai (inset), their spike threshold saturated at currents >200 pA. In sharp contrast, hilar inhibitory interneurons did not show a stimulus intensity-dependent increase in spike threshold (Fig. 4Aii) and the responses in both subtypes of

inhibitory neurons were not that different from each other (Kruskal-Wallis test: $p = 0.56$). A fixed, invariant threshold is what is typically expected and often modelled using the LIF formalism but since the opposite was observed, we had to resort to the slightly more complex EIF with added threshold dynamics (see below). These results outline a salient mechanism of hilar MCs and CA3 pyramidal wherein they adjust their spike threshold so that stronger excitatory synaptic inputs would presumably have to reach a higher threshold to initiate a spike (see Discussion).

For a neuron with a passive (RC) subthreshold membrane, a stronger stimulus current is expected to more rapidly charge the membrane capacitance resulting in a shorter first spike latency. In contrast, the increased spike threshold outlined above is expected to counteract this effect and increase latency. We therefore examined the latency to 1st spike as a function of current intensity to clarify the effect of a dynamic threshold on spike latency (Fig 4B,4C and Suppl. Fig. 1B). In CA1 pyramidal neurons, we found that increasing the stimulus current intensity caused a simple exponential decrease in spike latency (Fig. 4B; dark yellow curve), consistent with the relatively small increase in threshold observed over this current range. In contrast, the hilar MCs latencies to 1st spike was significantly different to those of the CA1 pyramidal neurons (multiple comparison (Dunn's test): $p = 0.017$) and was best captured by a linear fit. The greater increase in spike threshold for hMCs vs CA1 pyramidal cells may account for the smaller decrease in latency, but the very noisy hMC latency vs current plots suggest that other factors are operative. Surprisingly, CA3 pyramidal cell spike latencies were nearly independent of current intensity and their average distribution was significantly different from those of the hMC but not of the CA1 pyramidal neurons (Fig. 4Ci, Kruskal-Wallis test: $p = 7.3 \times 10^{-4}$; multiple comparison (Dunn's test): CA3 vs hMC: $p = 0.006$; CA3 vs CA1: $p = 0.99$). In contrast, the spike latency of both inhibitory subtypes showed little dependencies on the intensity of the current injection but were not significantly different from each other (Fig. 4Cii, Kruskal-Wallis test: PV vs SOM: $p = 0.22$). Thus, while hMC and CA3 pyramidal cells have comparable increases in threshold with increasing current injection (Fig. 4A) they differ markedly with respect to the effect of current intensity on spike latency (Fig.4Ci). This difference cannot be explained by the passive properties of these neurons, for example, the input resistance, since all of the tested excitatory cells, with the exception of the dentate GC, have very similar passive intrinsic properties (Table 1).

Altogether, we conclude thus far that the dynamic spike threshold and latency can be at least partly independently controlled by unknown subthreshold mechanisms. We further note that the latency of hilar inhibitory interneurons was far lower than that of hMCs, *i.e.*, a weak input to an inhibitory cell will initiate spiking at a shorter latency than a strong input to a hMC (compare Fig. 4B vs 4Cii).

Dynamic spike threshold in the hippocampal formation

Based on the analysis outlined above, it seems that the spike threshold is strongly regulated in hMCs and thus warrants further investigation if we were to include it into an experimentally-derived hMC model. When examining the first evoked spike from square-pulse current injections, we observed that the distribution of 1st spike thresholds in hMCs was shifted towards depolarized potentials after the addition of 10 μ M CNQX (N = 14 cells: Fig. 5Ai, 5Aii, 5Aiii, mean 1st spike threshold before CNQX: -48.1 ± 5.20 mV; after CNQX: -42.44 ± 6.90 mV; paired *t*-test: $p = 0.022$). Additionally, the spike threshold was not correlated with the variability of the resting membrane potential (linear fit: $y = -0.24x - 40.0$; adjusted R-square: -0.039 ; N = 14 cells: Fig. 5Aii). When we compared the average 1st spike threshold across the major hippocampal cell types, we found that the average 1st spike threshold of the hMC (mean 1st spike threshold: -42.5 ± 6.6 mV) was comparable to the other major hippocampal cell types tested (Table 1; Kruskal-Wallis: $p = 0.014$; multiple comparison test (Dunn's test): hMC vs GC: $p = 1.0$; hMC vs CA3: $p = 1.0$; hMC vs PV: $p = 0.89$; hMC vs SOM: $p = 0.54$; GC vs CA3: $p = 1.0$; PV vs SOM: $p = 1.0$; Fig. 5Aiii). The one exception was the CA1 pyramidal neurons which had a lower spike threshold (CA1, N = 7 cells, mean 1st spike threshold: -51.5 ± 3.6 mV) but this failed to reach significance in comparison to the hMC (multiple comparison test (Dunn's test); hMC vs CA1: $p = 0.082$), and all the other excitatory cell types (GC vs CA1: $p = 0.053$; CA3 vs CA1: $p = 0.17$; Fig. 5Aiii). This comparison reveals that that the excitatory and inhibitory cells within the hilar network have similar first spike thresholds.

Past *in vivo* studies have demonstrated that hMCs often displayed complex spiking patterns when the experimental animal (rat, mouse) traversed its place field (GoodSmith *et al.*, 2017; Senzai & Buzsaki, 2017). This prompted us to investigate whether there are other intrinsic mechanisms that could control the spiking behaviour of these cells. In addition to the AHP, a second intrinsic mechanism which could regulate spiking is a dynamic spike threshold (Trinh *et*

al., 2019). When examining the evoked spiking response, we noticed that the spike threshold increased after successive spiking (Fig. 5B). This adaptation was found in hMCs and all the other studied hippocampal cell types (Fig. 5C). This increase in spike threshold was significantly stronger in the hMC and GC neurons when compared to the PV inhibitory interneurons, but not to the other tested hippocampal cell types (Kruskal-Wallis test: $p = 0.014$; multiple comparison test (Dunn's test): GC vs hMC: $p = 1$; GC vs CA1: $p = 0.82$; GC vs PV: 0.038 ; GC vs SOM: $p = 0.97$; hMC vs CA1: $p = 0.66$; hMC vs PV: $p = 0.018$; hMC vs SOM: $p = 0.89$; PV vs SOM: $p = 0.50$; Fig. 5D, Suppl. Fig. 2A). CA3 pyramidal neurons were omitted in this analysis, given their inability to produce sufficient spiking for a valid comparison across cells (Fig. 5Cii).

To further characterize the adaptation dynamics of the spike threshold, we implemented a protocol to measure its recovery timescale. We used a ramp current injection protocol that was previously used to measure the decay of this adaptation process in hippocampal-like cells of a teleost fish (Trinh *et al.*, 2019). In short, a long ramp current was used to evoke spiking and consequently an increase in spike threshold (stimulus ramp). This was followed by the injection of a shorter and smaller ramp current used to evoke a single spike (probe ramp) at various time delays Δt independently of one another (from 50 ms to 1000 ms). This allowed us to analyse how the increase in spike threshold decays as a function of the inter-stimulus delay between the stimulus and probe ramps (Fig. 6Ai, 6Aii). In the case of the hMCs, the spike threshold relaxed back slowly to its resting state (Fig. 6Aiii), with a mean decay time constant = 570.4 ± 242.9 ms; $N = 12$ cells; (Fig. 6B; full recovery was not achieved at 1000 ms). Interestingly, the recovery timescale was similar to that reported for fish hippocampal-like neurons (Trinh *et al.*, 2019).

The GC displayed a sharp transient increase in spike threshold (Fig. 6Cii), but the recovery to baseline occurred by 50 ms (*i.e.*, either at or before the first probe ramp; $N = 9$ cells; Fig. 6C, 6D). CA3 pyramidal neurons displayed the strongest initial increase in spike threshold (CA3, $N = 7$ cells mean: 4.4 ± 2.8 mV at the first probe ramp) when compared to the other cell types (one-sided ANOVA: $p = 5.62 \times 10^{-5}$; multiple comparison test: CA3 vs GC: $p = 2.61 \times 10^{-5}$; CA3 vs CA1: $p = 0.016$; CA3 vs hMC: $p = 0.11$; CA3 vs PV: $p = 0.0053$; CA3 vs SOM: $p = 0.012$, Fig. 6B, 6E). In contrast, CA1 pyramidal neurons ($N = 7$ cells) and the inhibitory hilar cell types (PV: $N = 8$ cells, SOM: $N = 9$ cells) showed little increase in spike threshold following the stimulus ramp, *i.e.*, the delta spike threshold at the first probe ramp was ~ 1 mV (Fig. 6Eii, 6Eiii, 6Eiv).

All hippocampal cell types, except for the GC, were fitted with an exponential curve of the type: Delta spike threshold = $A \exp(-\Delta t/\tau)$, where A is a constant, Δt is the time delay between the stimulus and probe ramp, and τ is the decay time constant. This allowed us to estimate the average decay time constant (τ) of the spike threshold adaptation. Based on our fitting, the decay constant for the CA3 (mean τ : 462.6 ± 165.9 ms) and hMC (mean τ : 570.4 ± 242.9 ms) neurons were bigger than those of the other cell types (Fig. 6F, mean τ : CA1: 189.4 ± 68.9 ms; hilar SOM mean τ : 344.8 ± 237.5 ms; hilar PV mean τ : 157.8 ± 84.4 ms). When we compared the fitted curve of the spike threshold recovery across the different cell types, the hMC and CA3 pyramidal neurons were significantly slower (Kruskal-Wallis test: $p = 8.2 \times 10^{-16}$; multiple comparison test (Dunn's test): hMC vs GC; $p = 2.8 \times 10^{-11}$, hMC vs CA3; $p = 1.0$; hMC vs CA1: $p = 1.1 \times 10^{-4}$; hMC vs PV: $p = 6.7 \times 10^{-4}$; hMC vs SOM: $p = 0.088$; CA3 vs GC: $p = 2.1 \times 10^{-12}$, CA3 vs CA1: $p = 2.0 \times 10^{-5}$; CA3 vs PV: $p = 1.4 \times 10^{-4}$; CA3 vs SOM: $p = 0.03$; PV vs SOM: $p = 0.95$). In comparison to the other tested cells, the CA3 and hMC neurons displayed the most prominent spike threshold increase after the first (shortest delay) probe ramp, followed by a much slower recovery from adaptation (Fig. 6F). This might explain the hMC's sparse firing patterns *in vivo* (see Discussion).

An effective model for the threshold dynamics

Aiming at the future development of a hilar network model, we initially set out to develop a single cell model which captures salient excitability features of hMCs, such as their spike threshold dynamics (see Methods for model choice justification, and simulation details). During the fit process, we considered several variations of the leaky linear IF (LIF) model, and a few of them were good in fitting most of the experimental features observed in the hMCs (not shown). We also considered the AHP amplitude and ISI while adjusting the model. We started from a leaky IF with a simple spike-dependent dynamic threshold (Benda *et al.*, 2010). This base model is given in Eqs. (1)-(2) with the following simplifications: remove the exponential term in the membrane potential, replace the membrane reset expression by an absolute value V_R , and replace the input-dependent dynamic $\theta(t)$ by a constant θ_0 that represents the average initial threshold of hMCs. Then, the total threshold is $\theta(t) = \theta_0 + \theta_s(t)$, and the cell emits a spike whenever $V(t) = \theta(t)$. This model fitted the threshold increase versus spike number, but performed

poorly for all other features, since there is no dependency on the intensity of the injected current, nor covariance of the AHP with the threshold.

The first modification that we tried on the LIF was to replace the average initial threshold θ_0 by a variable $\theta(t)$ whose rate of change varied linearly with the membrane potential, $d\theta/dt \sim V$. This model has an analytical solution, and it can be shown that the first spike threshold decreases as the injected current increases (not illustrated), contrary to what is observed in hMCs. The observed dependence of the first spike threshold in Fig. 4A (inset) motivated the inclusion of a sigmoidal shape to $d\theta/dt$ that depended on the external current, rather than on V , as described in Eq. (1). The improved LIF with dynamic threshold then included this feature together with the linear resetting rule for V , resulting in a model almost equal to the one given by Eqs. (1) and (2), except for the exponential term in the membrane equation. This improved LIF also had an extra simplified K^+ -current for the AHP, $I_K = -g_K(V - E_K)$, with g_k obeying an equation similar to θ_s (a positive kick on the reset, followed by an exponential decay). This version had a very nice overall fit to most of the parameters and performed similarly to our modified EIF that we present in this section (see Figs. 7). However, the fit to both the threshold decay and to the first spike threshold could not be done simultaneously by the LIF.

We then decided to explore the EIF, since it has a more natural spike initiation, without the need of an artificial threshold (Fourcaud-Trocmé *et al.*, 2003). By introducing a novel dynamic into its threshold-related parameter, which controls the unstable fixed point of the underlying dynamics, we were able to reach a compromise between a good fit to both the threshold at spike initiation and the threshold decay. We were also able to drop the K^+ -current, which had been introduced for the leaky IF to enhance the AHP amplitude fitting. This is because the exponential dynamics adds more flexibility to the membrane potential equation and is capable of generating a sufficiently deep AHP without that explicit current.

The EIF fits to all the considered hMC features are detailed in Fig. 7. For example, the input-dependent part of the modified EIF threshold follows closely the hMC data. As expected, it presents a sigmoidal dependency on the injected current, saturating at around 200 pA (Fig. 7B). The latency, however, is underestimated for large currents, but matches the experimental data in the weakly excitable regime, when the injected current is very small (Fig. 7C). This is because hMCs tend to have a consistent delayed first spike, even though the delay slowly decreases with input intensity. The change of slope before the first spike in hMCs (as in the control condition of

Fig. 5Bii), as well as the underestimation of the first spike latency, suggest that there is an underlying mechanism delaying the first spike. To account for this fact, we tried implementing a simplified fast inactivating K^+ -current, also known as an I_A current, as proposed for serotonergic neurons in the raphe nucleus (Harkin *et al.*, 2021) since these currents are also known to be present in mossy fibre boutons (Geiger & Jonas, 2000). However, the I_A term caused the rheobase currents in our model to rise significantly, such that we were able to initiate spiking only for currents greater than 150 pA, contrary to what we observed in hMCs (some cells could spike with current injections as low as 20 pA – data not shown). The rheobase was defined as the minimal amount of current needed to produce an action potential. This suggests that a deeper scrutiny of the hMC peri-threshold membrane currents is necessary to be able to fully capture the delay to first spike.

In hMCs, the spike-dependent threshold increase is more consistent than in the modified EIF model (Fig. 7D): for small inputs (mean $\bar{I}_{ext} = 125$ pA), the spike-dependent threshold of hMCs grow almost as much as for large inputs (mean $\bar{I}_{ext} = 245$ pA). The model average threshold growth lies within the range observed experimentally. However, in the model the threshold is more flexible: it grows very little for small inputs (down-pointing triangles), but very much for large inputs (up-pointing triangles).

Our final model effectively reproduced the decay time constant of the hMCs (Fig. 7E, decay $\tau = 539 \pm 19$ ms for the model, and $\tau = 570 \pm 243$ ms for hMCs). The initial value for the decay (at the first 50 ms delay between ramps) is highly sensitive to the first (stimulus) ramp intensity, whereas the probe intensity influences the overall trend of the decay (higher intensities shift the observed decay curve upwards). This is because the model's threshold is directly influenced by the injected current, and it seems to grow more rapidly than the experimentally observed threshold, especially for high input currents (as shown in Fig. 7D). The sigmoidal dependence on the injected current in Eq. (1) plays an important role in shaping the threshold decay curve as well. This happens because the probe ramp used to measure the threshold values at subsequent delays, feeds back into the threshold itself, increasing it until a spike is emitted by the membrane voltage running off to infinity. We did not investigate the details of this feedback mechanism because we were interested in a model that captured the average behaviour of a hMC rather than the details of the underlying currents.

We plotted the minimum of the AHP versus the threshold of the spike that generated it (*i.e.*, the spike preceding that minimum – see Fig. 7F). These two quantities have a clear correlation in hMCs, motivating the linear reset rule we used in the model [upper expression in Eq. (2)]. A higher threshold implies that the spike occurs at a more depolarized membrane potential and therefore further from the potassium equilibrium potential. Thus, a stronger potassium driving force appears in the subsequent spike. In fact, the parameter $\alpha = 0.8$ (the slope of the reset potential) was directly extracted by fitting the experimental data with a straight line (pooling all spikes from all injected currents together – Fig. 7F inset). Notwithstanding, the slope of the model AHP-threshold covariance is almost constant at α , whereas the observed hMCs slope remains close to 0.8 over a large range of inputs, decreasing drastically for high inputs due to saturation effects in the membrane dynamics that were not included in the model.

We left detailed biophysical data out of the model because it is tailored for large-scale simulations of the circuitry involved in spatial learning and navigation. Thus, it is important to understand how some key parameters influence the features shown so far. Since the main novelty in our model is the threshold dynamics, we selected its parameters to check for robustness. We varied them within a range that produced mathematically valid outputs and show some examples in Fig. 8. All the four threshold-related features that we considered (threshold increase versus spike number and input, latency, and threshold decay) showed robust behaviour over variations in parameters. The AHP-threshold covariance was not significantly affected by the parameters in the θ and θ_s equations. The parameters that were the most robust were $\Delta\theta$, τ_θ and V_m . On the other hand, the model was more sensitive to alterations in the parameters of the $d\theta/dt$ equation, especially I_0 . The measured quantities that showed more marked variations with respect to parameter changes are the first spike threshold (Fig. 8A) and the threshold decay (Fig. 8D).

The default parameter set for our EIF model is given in Table 2. Some parameters in the table were fixed by experimental averages, and others were computed by adjusting the model curves to the experimental ones in Fig. 7. It represents an average hMC. Even though our model is robust to parameter variations, some changes tend to enhance the fitting to the threshold increase, but worsen the fit to the threshold decay, and *vice-versa*. This suggests that the hMCs have correlations between some of their membrane parameters due to correlations of the underlying channel kinetics. Since we were not interested in fitting a complete conductance-based model to the dynamics, we did not look into these correlations in further details. Instead, we simply added

a noise term to the membrane equation, generating some variability in the membrane potential simulations and feature statistics of the model behaviour, and thus capturing a component of the observed variation in hMCs experiments.

Discussion

We report herein a biophysical examination of hippocampal hilar neurons that identified the salient properties of hMCs, distinguishing them from the other targets of mossy fibres: hilar inhibitory interneurons and CA3 pyramidal cells. As discussed below, these distinguishing features of hMCs may be important for interpreting the differences in the responses of DG and CA3 neurons to spatial stimuli (Senzai & Buzsaki, 2017; GoodSmith *et al.*, 2019).

In comparison to inhibitory interneurons, hMCs displayed: 1) a robust increase in spike threshold with increasing input current that was accompanied by notably delayed spiking; 2) strong adaptation mechanisms consisting of a rapidly acting mAHP; and 3) a novel spike triggered-increase in spike threshold acting on a protracted time scale of hundreds of milliseconds. These specific spiking dynamics of hMCs and hilar inhibitory interneurons organized in a feedforward inhibitory motif converge in constraining the excitability of hMCs in response to synaptic inputs, consistent with their characteristic low firing rates *in vivo* (GoodSmith *et al.*, 2017; Senzai & Buzsaki, 2017). We further developed a cellular model that captures the excitability features and that is thus conducive to examine how the spiking behaviours of hMCs observed *in vivo*, and their resultant computations, emerge from the dynamics of their hilar synaptic inputs.

Our analysis of hilar interneurons moreover showed that their spiking behaviour (both 1st spike threshold adaptation and latency to 1st spike) are very stereotypical and do not vary as much as the excitatory cells. In contrast, CA3 pyramidal cells share many similar electrophysiological properties with hMCs, including the adaptative spike threshold. The CA3 pyramidal cells did differ from hMCs, however, in that their spike latency did not decrease with increasing injected current (Fig. 4Ci) and they exhibited far less membrane potential noise (Fig. 1D). These differences showcase the distinctive roles of these neurons in the hilar circuits.

The spike threshold of hMCs retains a memory of prior spikes (Fig. 5 and 6). Indeed, the spike threshold increased steeply over successive spikes making it increasingly difficult to drive spiking (Fig. 5B, 5C). A ramping current injection protocol (Trinh *et al.*, 2019) revealed that the

spike threshold of hMCs and CA3 pyramidal cells exhibited the more adaptable thresholds, increasing more and recovering more slowly – another similarity between these two neurons. The hMC spike-dependent increase in threshold extended for up to 1000 ms and therefore limits spiking over a timescale that is substantially longer than that of the mAHP. Although it is unknown what may be causing this particular spike threshold adaptation, the slow recovery from inactivation of Na⁺ channels has been previously suggested to be a possible biological mechanism for this process (Henze & Buzsaki, 2001; Platkiewicz & Brette, 2011; Trinh *et al.*, 2019). A more exhaustive study will be needed to fully dissect the mechanism of this particular dynamic spike threshold.

Synaptic noise in the hilar network

The striking amount of synaptic noise of hMC neurons in comparison to all the other tested hippocampal cells (Fig. 1D) raises an important question: what neurons contribute to this noise? Mossy cells receive input from DG granule and CA3 pyramidal cells; and both are known to fire very sparsely *in vivo* (Goodsmith *et al.*, 2017). The GCs project to both hMCs and CA3 pyramidal cells and coupling of action potentials to synaptic release is shared across these cell types (Marosi *et al.*, 2023), implying that the GC driven noise should be similar in both of these synaptic targets. Given the very low membrane noise levels of CA3 pyramidal cells (Fig. 1D) it therefore appears unlikely that GCs are a major source of hMC noise. Two lines of evidence suggest that CA3 pyramidal cells are also unlikely to be the source of hMC synaptic noise. First, CA3 pyramidal cells are recurrently connected and, if they were the noise source, it would be expected that they too would exhibit an equal amount of noise. Second, the CA3-hMC synapse is also known to have a high failure rate (Scharfman, 1994b) and cutting the CA3 to hMC fibres does not decrease hMC noise (Hedrick *et al.*, 2017). Earlier studies provided no decisive evidence on whether hMCs are recurrently connected (Buckmaster *et al.*, 1996; Sun *et al.*, 2017). However, recent studies have shown that hMCs are synaptically connected (Larimer & Strowbridge, 2008; Ma *et al.*, 2021) and a hMC recurrent network is therefore a strong possibility as the noise source. The Poisson or renewal property of the synaptic noise might then simply be due to independence release from multiple recurrent connections and the low firing rates of hMCs (in our slices: 6.3 ± 3.6 Hz). Clearly, much more work will be required to clarify the implications of the high levels of hMC synaptic noise for hMC function *in vivo*.

Efficient dynamical model for hMCs

We developed a model that captures important experimentally-derived excitability properties of hMCs. No other model has been designed specifically for hMCs, and many of our model features are innovative with respect to the more general neural modelling literature. It addresses the interplay of standard spike-driven adaptation with hMC-specific nonlinearities (such as the AHPs, the latencies, and the input-dependent spike threshold increase). One important feature of this model is the implementation of a realistic threshold that mimics both the positive feedback characteristics of the Na^+ channel activation and the complex kinetics of its recovery from inactivation. We lack, however, biophysical insights into the input-dependent threshold of the first spike and its relation to SK channel gating that generates the AHP. The latency to first spike is a consequence of these dynamical effects, and more detailed biophysical analyses will be required to better capture threshold dependence on natural synaptic input patterns. The formulation of our equations enables easy incorporation of other kinetics and currents that future biophysical studies may reveal.

The dynamics of our model readily predicts that the substantial and protracted spike threshold increase following spiking in hMCs impedes high frequency firing. The AHP has the same effect and augments the increased threshold by its positive covariation with the most recent threshold value (Fig. 7F), *i.e.*, increasing threshold and the concomitant increase in the AHP will act synergistically to limit hMC discharge. These two adaptation mechanisms operate over distinct timescales and are therefore modulating excitability under distinct running average estimates of spike timing. More importantly perhaps, our data could be well-fitted without the need for dynamical ingredients that cause intrinsic bursting, *i.e.*, recurring bouts of high frequency firing for constant input. Higher frequencies are seen here at the onset of step currents, as is expected for adaptation processes that are known to preferentially encode changes in input strengths (*i.e.*, their temporal derivative).

Our parsimonious cellular model is computationally efficient since it involves a small number of variables and no transcendental function evaluations. It does not require a time step small enough to properly simulate the fast-varying voltage during an action potential either. Instead, this modified integrate-and-fire-type equation inserts a spike and resets the voltage upon fulfilment of a mathematical threshold condition. Hence it is ideal for inclusion in broader

network models involving multiple hMCs. This will allow deeper investigations into the effects on hippocampal function of connections between hMCs (Ma *et al.*, 2021), of the reciprocal hMC to GC connectivity with associated hilar inhibitory interneurons, and of plasticity behaviours (Hashimoto *et al.*, 2017). This modelling framework will thus allow the teasing out of the role of the computations supported by hMCs in the context of pattern separation, completion and spatial learning.

Implications for *in vivo* studies of hMCs

While there are far fewer hMCs than GCs (Amaral *et al.*, 1990), they nonetheless occupy a privileged position in the hippocampal network. Mossy fibre collaterals from GC provide a major input to the hilus where they are believed to terminate onto proximal dendritic excrescences of a small number hMCs as well as onto local inhibitory interneurons (Acsády *et al.*, 1998). CA3 pyramidal cells project back to hMC distal dendrites and local inhibitory interneurons (Scharfman, 1994b; Kneisler & Dingledine, 1995) giving rise to the idea that hMCs act as comparator of its GC input and its CA3 feedback. The hMCs then feedback to a widespread population of GCs directly (Scharfman *et al.*, 1990; Scharfman, 1995) and via inhibitory interneurons (Scharfman, 1995); *i.e.*, the GC/CA3 pyramidal cell “comparator” now presumably modulates its own input and therefore GC pattern separation and place field responses. From these well described connectivity features, several questions naturally arise, notably on how the putative comparator role of hMC emerges from their excitability dynamics. First, how will a hMC respond to the discharge of GC mossy fibre (Scharfman *et al.*, 1990; Scharfman, 1993) and CA3 pyramidal cells (Scharfman, 1994b, a), separately and in conjunction? Second, what is the effect of hMC spiking on their target GC discharge? The combination of a strong mAHP, dynamic threshold and rapid inhibition suggest that hMC spiking behaviour is, as a general feature, powerfully constrained, making unclear the magnitude of their influence on GCs excitability.

Granule cells often fire high frequency bursts in their place field (GoodSmith *et al.*, 2017). Since mossy fibres input to hMCs are strongly facilitating (Scharfman *et al.*, 1990; Lysetskiy *et al.*, 2005; Hedrick *et al.*, 2017; Lituma *et al.*, 2021) and can drive spiking when presented as bursts (Scharfman *et al.*, 1990), hMCs are thus expected to track the bursting of incoming GCs, for instance during spatial navigation. Direct evidence for this supposition comes from paired *in*

in vivo recordings of GCs and hMCs that shows that the probability of spike transmission rises strongly by the third spike of a burst (Senzai & Buzsaki, 2017). Likewise, the CA3 to hMC synaptic inputs are also facilitating (Scharfman, 1994b; Hedrick *et al.*, 2017). Thus, given the strong facilitatory short-term dynamics of both major excitatory inputs to hMCs, one would expect that a hMC would discharge at high rates as a rodent traversed its place field. This however does not appear to be the case: *in vivo* recordings show hMC firing rates ranging between 8 to 12 Hz in their place field (GoodSmith *et al.*, 2017). The translation of strongly facilitating GC and CA3 pyramidal cell synaptic input to only low frequency hMC discharge may thus be the direct result of the hMC dynamics described in this work. The combined actions of a strong mAHP acting over a short time scale and a dynamic threshold acting over a longer time scale are likely to dynamically modulate the encoding features of hMCs in response to synaptic inputs. Strong synaptic inputs are expected to lead to a higher spiking threshold, effectively encoding the onset of GC spike bursts, while filtering out the effects sustained GC spiking. Finally, the lower spike threshold for hilar inhibitory interneurons compared to hMCs suggests that the prominent inhibitory input to hMCs (Acsady *et al.*, 1998; Larimer & Strowbridge, 2008) will precede or overlap their excitatory input and further suppress their discharge. We hypothesize that these collective dynamics not only contribute to the low firing frequency of hMC discharge observed *in vivo*, but more specifically confers on hMCs the ability to preferentially encode the onset of GC burst spiking during navigation.

Implications for the function of hMC feedback to dentate granule cells

The hMC to GC synapses are weak and mostly masked by strong feed-forward inhibition (Scharfman, 1995; Hashimotodani *et al.*, 2017). A recent study (Hashimotodani *et al.*, 2017) has shown that hMC projections to GCs, but not to inhibitory interneurons, undergo strong presynaptic LTP as long as hMC fire multiple bursts (at frequencies >30 Hz). Following potentiation, burst stimulation of hMC axons strongly drive GCs. These results raise a critical question: under what conditions can hMC firing rates increase to the point at which LTP is induced, and can they effectively drive GC discharge? We suggest that there are two requirements for hMCs to strongly activate their GC targets: firstly, their excitability must be raised (Anderson & Strowbridge, 2014) to allow them to discharge at rates >30 Hz and, secondly, their input to GCs must be potentiated (Hashimotodani *et al.*, 2017).

Altogether, our results demonstrate that salient features of the *in vivo* behaviour of mossy cells can be traced back to the dynamics of the intrinsic properties that we have identified when put together with the synaptic inputs of the DG network, namely from GCs, CA3 pyramidal cells and inhibitory interneurons. Our key findings are that, at least *in vitro*, it is hard to induce spiking in hMCs and even harder to evoke sustained spiking. A critical next step will be to quantitatively compare the spiking statistics of hMCs when driven by spatial input (GoodSmith *et al.*, 2017; Senzai & Buzsaki, 2017) versus current injections *in vitro*. We anticipate that iterative implementations of our experimentally-driven model will allow us to better understand how hMC biophysics operates during navigation and spatial learning.

References

- Acsady L, Kamondi A, Sik A, Freund T & Buzsaki G. (1998). GABAergic cells are the major postsynaptic targets of mossy fibers in the rat hippocampus. *J Neurosci* **18**, 3386-3403.
- Alle H & Geiger JR. (2006). Combined analog and action potential coding in hippocampal mossy fibers. *Science* **311**, 1290-1293.
- Amaral DG. (1978). A Golgi study of cell types in the hilar region of the hippocampus in the rat. *J Comp Neurol* **182**, 851-914.
- Amaral DG, Ishizuka N & Claiborne B. (1990). Neurons, numbers and the hippocampal network. *Prog Brain Res* **83**, 1-11.
- Anderson RW & Strowbridge BW. (2014). Regulation of persistent activity in hippocampal mossy cells by inhibitory synaptic potentials. *Learn Mem* **21**, 263-271.
- Azouz R & Gray CM. (2000). Dynamic spike threshold reveals a mechanism for synaptic coincidence detection in cortical neurons in vivo. *Proc Natl Acad Sci U S A* **97**, 8110-8115.
- Benda J, Maler L & Longtin A. (2010). Linear Versus Nonlinear Signal Transmission in Neuron Models With Adaptation Currents or Dynamic Thresholds. *Journal of Neurophysiology* **104**, 2806-2820.
- Buckmaster PS & Schwartzkroin PA. (1994). Hippocampal mossy cell function: a speculative view. *Hippocampus* **4**, 393-402.
- Buckmaster PS & Schwartzkroin PA. (1995). Interneurons and inhibition in the dentate gyrus of the rat in vivo. *J Neurosci* **15**, 774-789.

- Buckmaster PS, Strowbridge BW & Schwartzkroin PA. (1993). A comparison of rat hippocampal mossy cells and CA3c pyramidal cells. *J Neurophysiol* **70**, 1281-1299.
- Buckmaster PS, Wenzel HJ, Kunkel DD & Schwartzkroin PA. (1996). Axon arbors and synaptic connections of hippocampal mossy cells in the rat in vivo. *J Comp Neurol* **366**, 271-292.
- Bui AD, Nguyen TM, Limouse C, Kim HK, Szabo GG, Felong S, Maroso M & Soltesz I. (2018). Dentate gyrus mossy cells control spontaneous convulsive seizures and spatial memory. *Science* **359**, 787-790.
- Cembrowski MS, Wang L, Sugino K, Shields BC & Spruston N. (2016). Hipposeq: a comprehensive RNA-seq database of gene expression in hippocampal principal neurons. *eLife* **5**, e14997.
- Danielson NB, Turi GF, Ladow M, Chavlis S, Petrantonakis PC, Poirazi P & Losonczy A. (2017). In Vivo Imaging of Dentate Gyrus Mossy Cells in Behaving Mice. *Neuron* **93**, 552-559 e554.
- Diamantaki M, Frey M, Berens P, Preston-Ferrer P & Burgalossi A. (2016). Sparse activity of identified dentate granule cells during spatial exploration. *Elife* **5**.
- Elliott SB, Harvey-Girard E, Giassi AC & Maler L. (2017). Hippocampal-like circuitry in the pallium of an electric fish: Possible substrates for recursive pattern separation and completion. *J Comp Neurol* **525**, 8-46.
- Ellis LD, Mehaffey WH, Harvey-Girard E, Turner RW, Maler L & Dunn RJ. (2007). SK channels provide a novel mechanism for the control of frequency tuning in electrosensory neurons. *J Neurosci* **27**, 9491-9502.
- Engel J, Schultens HA & Schild D. (1999). Small conductance potassium channels cause an activity-dependent spike frequency adaptation and make the transfer function of neurons logarithmic. *Biophys J* **76**, 1310-1319.

- Faisal AA, Selen LP & Wolpert DM. (2008). Noise in the nervous system. *Nat Rev Neurosci* **9**, 292-303.
- Fotowat H, Lee C, Jun JJ & Maler L. (2019). Neural activity in a hippocampus-like region of the teleost pallium is associated with active sensing and navigation. *Elife* **8**.
- Fourcaud-Trocmé N, Hansel D, van Vreeswijk C & Brunel N. (2003). How Spike Generation Mechanisms Determine the Neuronal Response to Fluctuating Inputs. *The Journal of Neuroscience* **23**, 11628-11640.
- Geiger JRP & Jonas P. (2000). Dynamic Control of Presynaptic Ca²⁺ Inflow by Fast-Inactivating K⁺ Channels in Hippocampal Mossy Fiber Boutons. *Neuron* **28**, 927-939.
- Gewaltig M-O & Diesmann M. (2007). NEST (NEural Simulation Tool). *Scholarpedia* **2**, 1430.
- Girardi-Schappo M, Bortolotto GS, Stenzinger RV, Gonsalves JJ & Tragtenberg MHR. (2017). Phase diagrams and dynamics of a computationally efficient map-based neuron model. *PLOS ONE* **12**, e0174621.
- GoodSmith D, Chen X, Wang C, Kim SH, Song H, Burgalossi A, Christian KM & Knierim JJ. (2017). Spatial Representations of Granule Cells and Mossy Cells of the Dentate Gyrus. *Neuron* **93**, 677-690 e675.
- GoodSmith D, Lee H, Neunuebel JP, Song H & Knierim JJ. (2019). Dentate Gyrus Mossy Cells Share a Role in Pattern Separation with Dentate Granule Cells and Proximal CA3 Pyramidal Cells. *J Neurosci* **39**, 9570-9584.
- Harkin EF, Payeur A, Lynn MB, Boucher J-F, Caya-Bissonnette L, Cyr D, Stewart C, Longtin A, Naud R & Béique J-C. (2021). Temporal derivative computation in the dorsal raphe network revealed by an experimentally-driven augmented integrate-and-fire modeling framework. *bioRxiv*, 2021.2006.2025.449907.

- Hashimotodani Y, Nasrallah K, Jensen KR, Chavez AE, Carrera D & Castillo PE. (2017). LTP at Hilar Mossy Cell-Dentate Granule Cell Synapses Modulates Dentate Gyrus Output by Increasing Excitation/Inhibition Balance. *Neuron* **95**, 928-943 e923.
- Hedrick TP, Nobis WP, Foote KM, Ishii T, Chetkovich DM & Swanson GT. (2017). Excitatory Synaptic Input to Hilar Mossy Cells under Basal and Hyperexcitable Conditions. *eNeuro* **4**.
- Henze DA & Buzsaki G. (2001). Action potential threshold of hippocampal pyramidal cells in vivo is increased by recent spiking activity. *Neuroscience* **105**, 121-130.
- Honeycutt RL. (1992). Stochastic Runge-Kutta algorithms. I. White noise. *Physical Review A* **45**, 600-603.
- Jinde S, Zsiros V, Jiang Z, Nakao K, Pickel J, Kohno K, Belforte JE & Nakazawa K. (2012). Hilar mossy cell degeneration causes transient dentate granule cell hyperexcitability and impaired pattern separation. *Neuron* **76**, 1189-1200.
- Kneisler TB & Dingledine R. (1995). Synaptic input from CA3 pyramidal cells to dentate basket cells in rat hippocampus. *J Physiol* **487**, 125-146.
- Kohler M, Hirschberg B, Bond CT, Kinzie JM, Marrion NV, Maylie J & Adelman JP. (1996). Small-conductance, calcium-activated potassium channels from mammalian brain. *Science* **273**, 1709-1714.
- Langston RF, Ainge JA, Couey JJ, Canto CB, Bjerknes TL, Witter MP, Moser EI & Moser MB. (2010). Development of the spatial representation system in the rat. *Science* **328**, 1576-1580.
- Larimer P & Strowbridge BW. (2008). Nonrandom local circuits in the dentate gyrus. *J Neurosci* **28**, 12212-12223.

- Lee KF, Soares C, Thivierge JP & Beique JC. (2016). Correlated Synaptic Inputs Drive Dendritic Calcium Amplification and Cooperative Plasticity during Clustered Synapse Development. *Neuron* **89**, 784-799.
- Leutgeb JK, Leutgeb S, Moser MB & Moser EI. (2007). Pattern separation in the dentate gyrus and CA3 of the hippocampus. *Science* **315**, 961-966.
- Lituma PJ, Kwon HB, Alvina K, Lujan R & Castillo PE. (2021). Presynaptic NMDA receptors facilitate short-term plasticity and BDNF release at hippocampal mossy fiber synapses. *Elife* **10**.
- Lysetskiy M, Foldy C & Soltesz I. (2005). Long- and short-term plasticity at mossy fiber synapses on mossy cells in the rat dentate gyrus. *Hippocampus* **15**, 691-696.
- Ma Y, Bayguinov PO, McMahon SM, Scharfman HE & Jackson MB. (2021). Direct synaptic excitation between hilar mossy cells revealed with a targeted voltage sensor. *Hippocampus* **31**, 1215-1232.
- Marcoux CM, Clarke SE, Nesse WH, Longtin A & Maler L. (2016). Balanced ionotropic receptor dynamics support signal estimation via voltage-dependent membrane noise. *J Neurophysiol* **115**, 530-545.
- Marosi EL, Arszovszki A, Brunner J & Szabadics J. (2023). Similar Presynaptic Action Potential-Calcium Influx Coupling in Two Types of Large Mossy Fiber Terminals Innervating CA3 Pyramidal Cells and Hilar Mossy Cells. *eNeuro* **10**.
- Marr D. (1971). Simple memory: a theory for archicortex. *Philos Trans R Soc Lond B Biol Sci* **262**, 23-81.
- McNaughton BL & Morris RG. (1987). Hippocampal synaptic enhancement and information storage within a distributed memory system. *Trends in neurosciences* **10**, 408-415.

- Neunuebel JP & Knierim JJ. (2014). CA3 retrieves coherent representations from degraded input: direct evidence for CA3 pattern completion and dentate gyrus pattern separation. *Neuron* **81**, 416-427.
- Platkiewicz J & Brette R. (2011). Impact of fast sodium channel inactivation on spike threshold dynamics and synaptic integration. *PLoS Comput Biol* **7**, e1001129.
- Rolls ET, Treves A & Rolls ET. (1998). *Neural networks and brain function*, vol. 572. Oxford university press Oxford.
- Scharfman HE. (1991). Dentate hilar cells with dendrites in the molecular layer have lower thresholds for synaptic activation by perforant path than granule cells. *J Neurosci* **11**, 1660-1673.
- Scharfman HE. (1992). Differentiation of rat dentate neurons by morphology and electrophysiology in hippocampal slices: granule cells, spiny hilar cells and aspiny 'fast-spiking' cells. *Epilepsy Res Suppl* **7**, 93-109.
- Scharfman HE. (1993). Characteristics of spontaneous and evoked EPSPs recorded from dentate spiny hilar cells in rat hippocampal slices. *J Neurophysiol* **70**, 742-757.
- Scharfman HE. (1994a). EPSPs of dentate gyrus granule cells during epileptiform bursts of dentate hilar "mossy" cells and area CA3 pyramidal cells in disinhibited rat hippocampal slices. *J Neurosci* **14**, 6041-6057.
- Scharfman HE. (1994b). Evidence from simultaneous intracellular recordings in rat hippocampal slices that area CA3 pyramidal cells innervate dentate hilar mossy cells. *J Neurophysiol* **72**, 2167-2180.
- Scharfman HE. (1995). Electrophysiological evidence that dentate hilar mossy cells are excitatory and innervate both granule cells and interneurons. *J Neurophysiol* **74**, 179-194.

- Scharfman HE. (2016). The enigmatic mossy cell of the dentate gyrus. *Nat Rev Neurosci* **17**, 562-575.
- Scharfman HE, Kunkel DD & Schwartzkroin PA. (1990). Synaptic connections of dentate granule cells and hilar neurons: results of paired intracellular recordings and intracellular horseradish peroxidase injections. *Neuroscience* **37**, 693-707.
- Scharfman HE & Myers CE. (2012). Hilar mossy cells of the dentate gyrus: a historical perspective. *Frontiers in neural circuits* **6**, 106.
- Sekerli M, Del Negro CA, Lee RH & Butera RJ. (2004). Estimating action potential thresholds from neuronal time-series: new metrics and evaluation of methodologies. *IEEE Trans Biomed Eng* **51**, 1665-1672.
- Senzai Y & Buzsaki G. (2017). Physiological Properties and Behavioral Correlates of Hippocampal Granule Cells and Mossy Cells. *Neuron* **93**, 691-704 e695.
- Stimberg M, Brette R & Goodman DFM. (2019). Brian 2, an intuitive and efficient neural simulator. *eLife* **8**, e47314.
- Sun Y, Grieco SF, Holmes TC & Xu X. (2017). Local and Long-Range Circuit Connections to Hilar Mossy Cells in the Dentate Gyrus. *eNeuro* **4**.
- Teeter C, Iyer R, Menon V, Gouwens N, Feng D, Berg J, Szafer A, Cain N, Zeng H, Hawrylycz M, Koch C & Mihalas S. (2018). Generalized leaky integrate-and-fire models classify multiple neuron types. *Nature Communications* **9**, 709.
- Ting JT, Daigle TL, Chen Q & Feng G. (2014). Acute Brain Slice Methods for Adult and Aging Animals: Application of Targeted Patch Clamp Analysis and Optogenetics. In *Patch-Clamp Methods and Protocols*, ed. Martina M & Taverna S, pp. 221-242. Springer New York, New York, NY.

- Trinh A-T, Clarke SE, Harvey-Girard E & Maler L. (2019). Cellular and Network Mechanisms May Generate Sparse Coding of Sequential Object Encounters in Hippocampal-Like Circuits. *eneuro* **6**, ENEURO.0108-0119.2019.
- Wills TJ, Cacucci F, Burgess N & O'Keefe J. (2010). Development of the hippocampal cognitive map in preweanling rats. *Science* **328**, 1573-1576.
- Yassa MA, Lacy JW, Stark SM, Albert MS, Gallagher M & Stark CE. (2011). Pattern separation deficits associated with increased hippocampal CA3 and dentate gyrus activity in nondemented older adults. *Hippocampus* **21**, 968-979.
- Yassa MA & Stark CE. (2011). Pattern separation in the hippocampus. *Trends Neurosci* **34**, 515-525.
- Zhang Y & Huang H. (2017). SK Channels Regulate Resting Properties and Signaling Reliability of a Developing Fast-Spiking Neuron. *J Neurosci* **37**, 10738-10747.

Additional Information

Data availability statement:

All data supporting the results presented in this manuscript are included in the manuscript figures as per the statistical policy of J. Physiol and are available upon request. All codes related to the EIF model will be available upon request and they are also made available at the Github repository (<https://github.com/mgirardis/mossy-cell-dg>).

Competing interest:

The authors declare no competing financial interest.

Author Contributions:

All experiments were done in the laboratories of J-C B, A L and L M at the University of Ottawa, Canada.

A-T T participated in the design of the experiments, acquired, analysed, and interpreted the data and wrote the manuscript.

M G-S constructed the computational model, analysed, and interpreted the data and wrote the manuscript.

J-C B designed the experiments, interpreted the data, and reviewed the manuscript for important intellectual content.

A L designed the experiments, interpreted the data, and reviewed the manuscript for important intellectual content.

L M designed the experiments, interpreted the data, and reviewed the manuscript for important intellectual content.

All authors have:

- approved the final version of the manuscript.
- agreed to be accountable for all aspects of the work in ensuring that questions related to the accuracy or integrity of any part of the work are appropriately investigated and resolved.

All persons designated as authors qualify for authorship, and all those who qualify for authorship are listed.

Funding:

This work was supported by the Canadian Institutes for Health Research Grant # 153143 to J-C B, A L and L M and by the Brockhouse award funds (493076-2017) to A L and L M and an NSERC award (RGPIN/06204-2014) to A L and a grant from the Krembil Foundation to J-C B, A L and L M.

Acknowledgements:

We would like to thank Dr. Kirk Mulatz for his help with technical support and Dr. Érik Harvey-Girard with his help in developing a cutting procedure which allowed us to record from the hilar mossy cells *in vitro*. We would also like to thank Ryan Sudhakar for his help in patching dentate

This manuscript was first published as a preprint: Trinh, A. T., Girardi-Schappo, M., Béique, J. C., Longtin, A., & Maler, L. (2022). Dentate gyrus mossy cells exhibit sparse coding via adaptive spike threshold dynamics. *bioRxiv*. <https://doi.org/10.1101/2022.03.07.483263>

granule cells and finally Dr. Timal Kannangara with his help with the voltage clamp experiments.

Supporting Information

Supplementary Figure 1. Stimulus dependent biophysical characteristics. Extended data for figure 4.

A. The first spike threshold for all of the recorded cells was plotted as a function of the stimulus current intensities. All data points are shown in individual plots for clarity. Filled symbols are individual recorded values while open symbols are the averaged values used in Fig 4. (Linear fits for GC: $y = 0.084x - 50.98$, CA3: $y = 0.076x - 54.59$, hMC: $y = 0.089x - 56.93$, CA1: $y = 0.04x - 55.93$, PV: $y = -0.015x - 48.17$, SOM: $y = 0.0057x - 50.47$). **B.** The latency to 1st spike for all of the recorded cells was plotted as a function of the stimulus current intensities. All data points are shown in individual plots for clarity. (Exponential fit for CA1: $y = 1279.3 * e^{-x/44.2} - 25.6$, Linear fits for GC: $y = -0.92x + 195.36$, CA3: $y = -0.14x + 123.9$, PV: $y = -0.49x + 111.76$, SOM: $y = -0.27x + 109.94$). Colour scheme: GC (N= 9 cells): dark blue filled squares; CA3 (N= 8 cells): yellow triangles, CA1 (N= 7 cells): magenta pentagons; hMC (N= 14 cells): teal circles; hilar PV (N= 8 cells): pink circles; hilar SOM (N= 9 cells): cyan squares. The shaded area corresponds to the standard deviation.

Supplementary Figure 2. Dynamic spike threshold dynamics across hippocampal cell types.

Extended data for figure 5. **A.** The increase in spike threshold (delta spike threshold) was plotted as a function of the spike number. For the hMC neurons, only 1 cell (N=1) had >10 spikes. Colour scheme: GC (N= 9 cells): dark blue filled squares; CA3 (N= 8 cells): yellow triangles, CA1 (N= 7 cells): magenta pentagons; hMC (N= 14 cells): teal circles; hilar PV (N= 8 cells): pink circles; hilar SOM (N= 9 cells): cyan squares. The shaded area denotes the standard deviation.

Tables

Table 1. Summary table of the intrinsic parameters of the different hippocampal cell types. All spike parameter values were obtained from examining the first evoked spike from a square-pulse current injection and by averaging across all tested current intensities.

Cell types	GC	hMC	CA3	CA1	Hilar PV	Hilar SOM
Membrane Parameters	N = 9 cells	N = 14 cells	N = 8 cells	N = 7 cells	N = 8 cells	N = 9 cells
Resting Membrane Potential (mV)	-74.7 ± 5.3	-64.6 ± 10.4	-70.0 ± 5.3	-70.7 ± 5.5	-65.1 ± 4.8	-60.6 ± 9.1
Input Resistance (MΩ)	629.4 ± 273.0	257.3 ± 69.3	302.0 ± 94.4	290.9 ± 34.3	259.0 ± 140.5	265.0 ± 254.1
Membrane Time Constants (ms)	20.9 ± 5.8	36.4 ± 16.3	49.3 ± 25.7	29.6 ± 6.5	30.1 ± 15.6	29.6 ± 8.9
Spike Parameters						
Spike Amplitude (mV)	114.7 ± 8.1	104.4 ± 8.6	98.2 ± 14.8	111.3 ± 7.0	89.9 ± 13.7	98.2 ± 13.6
Latency to 1st spike (ms)	137.1 ± 77.2	208.1 ± 53.8	100.8 ± 69.7	133.2 ± 41.6	76.4 ± 43.3	67.9 ± 35.2
Spike Threshold (mV)	-40.5 ± 7.7	-42.5 ± 6.6	-41.9 ± 7.6	-51.5 ± 3.6	-47.5 ± 7.3	-48.0 ± 6.7
Spike Half-width (ms)	1.9 ± 0.2	2.1 ± 0.4	2.3 ± 0.7	2.0 ± 0.2	0.9 ± 0.3	1.2 ± 0.5
AHP Amplitude (mV)	6.5 ± 4.0	8.1 ± 3.0	3.8 ± 5.2	3.4 ± 1.1	10.5 ± 5.6	11.6 ± 7.1

Table 2. Model parameters obtained by simulating the model and comparing the following features with experimental data: threshold increase versus spike number, threshold of the first spike versus input current, threshold decay, the covariance between AHP minimum and spike threshold, and the latency to the first spike. These values reflect an average hMC and generate curves that match the experimental observations within error bars in Figure 7. Finding a parameter set that matches a specific hMC would further require considering possible correlations between the parameters given here, and is beyond the scope of our work.

* Parameters estimated by averaging hMC's corresponding features. Values slightly differ from those of Table 1 because we used a smaller sample of hMCs here.

Other parameters correspond to simplifications of the complex hMC currents, so they have no direct corresponding quantities in electrophysiological measurements. They have been adjusted by hand to yield the fits in Figure 7.

Parameter	Description	Parameter	Description
$V_b = -67$ mV	* Resting membrane potential	$k = 0.1$ mV	Spike slope
$R = 150$ M Ω	Membrane resistance	$\tau = 38$ ms	* Membrane time constant
$\sigma = 0.5$ mV	* White noise strength	I_{ext}	External input
$\tau_1 = 20$ ms	Threshold activation time constant	$V_0 = -48.5$ mV	* Threshold baseline
$s = 13.44$ mV	Threshold activation amplitude	$R_\theta = 20$ M Ω	Threshold-input coupling resistance
$I_0 = 120$ pA	Threshold activation half current	$\Delta\theta = 2$ mV	Spike threshold increment
$V_m = 30$ mV	Spike-dependent threshold saturation	$\tau_\theta = 300$ ms	Threshold decay time
$\alpha = 0.8$	* Reset voltage slope	$\delta = 2$ mV	Reset voltage drop
$V_{peak} = -20$ mV	Threshold for resetting		

Figures legends

Figure 1. Strong membrane fluctuations are present in hMC neurons. **A.** Example of a cell displaying spontaneous spiking at a rate of 2.2 Hz. Multiple spontaneous events can be seen prior to spiking (inset). **B.** Postsynaptic potential amplitude histogram for the example trace shown in **A**. Analysis of the postsynaptic potentials reveals that most spikes occur during spontaneous events having greater than 12 mV in amplitude as denoted by the arrows. **C.** Average normalized membrane fluctuations histogram. **D.** Comparison of membrane potential variance across hippocampal cell types. **E.** Example current clamp traces of the hMC membrane potential following the application of synaptic blockers. **Ei)** The application of a glutamate AMPA receptor blocker, 10 μ M CNQX, completely abolishes the generation of spontaneous events (bottom, red trace). **Eii)** In contrast, the bath application of a GABA_A antagonist, 0.1 mM PTX, did not appear to strongly affect the generation of spontaneous events. **F.** Summary of the MP variance following the bath application of synaptic blockers in current. **Fi)** MP variance after the application of CNQX. (N = 14 cells) **Fii)** MP variance after the application of PTX. Each grey dashed line series represents an experiment, while each open circle represents the average for a given cell. The open circle black-red pair indicates the cell used in **1E**, while the filled black circle represents the average across cells (N = 4 cells). **G.** Example voltage clamp trace before (upper panel) and after (lower panel) the application of 0.1mM PTX. **H.** Example current-clamp traces of an hMC neuron following depolarizing current injections. Even at higher membrane potentials, the observed postsynaptic potential events were all positive deflections (inset). n.s. = non-significant, *** p<0.001.

Figure 2. Spiking independent synaptic noise. **Ai)** Example of a voltage-clamp trace of an hMC neurons. A magnified version of the recording trace denoted by the shaded grey area is highlighted in **Aii)**. **Bi)** Example of a voltage-clamp trace after the application of 0.5 μ M TTX. A magnified version of the recording trace denoted by the shaded grey area was highlighted in **Bii)**. **C.** EPSC amplitude plot. **D.** Average EPSC event frequency plot. **E.** Inter-event serial correlation plot. Each grey dash line series represents an experiment while each open circle represents the average for a given cell. The open circle black-red pair indicates the cell used in **2A** and **2B** while the filled black circle represents the average across all cells (N = 7 cells). **F.** Histogram of inter-event intervals. The cumulative probability plot is also shown in the inset. n.s. = non-significant, ** p<0.01

Figure 3. Characterizing the AHP in hMC neurons. **Ai)** Example neuronal response to +270 pA square pulse current injections. **Aii)** Same as in **Ai)**, except that 10 μ M CNQX has been applied prior to this recording. Notice that the AHP becomes more distinguishable in the absence of synaptic noise (black arrow). **Bi)** Left: Example response trace following a 500 ms square-pulse current injection in the presence of PTX and CNQX. A magnified view of the AHP defined by the dark grey zone (left) is shown in the inset on the right. Inset: The medium component of the AHP (mAHP) is defined by the light grey zone. The black arrow illustrates the trough of the AHP. **Bii)** Example current-clamp trace illustrating the reduction of the AHP following the bath application of UCL1684. This also reduced the 1st spike threshold by ~3.0 mV and slightly depolarized the membrane potential as denoted by the black arrow (end of the trace). **C.** 1st spike mAHP area plot. **D.** 1st spike AHP amplitude plot. Each grey dashed line represents an experiment while each open circle represents the average for a given cell. The open circle black-red pair indicates the cell used in **Bii)** while the filled black circle represents the average across all cells (N = 6 cells). * p < 0.05.

Figure 4. Stimulus dependent biophysical characteristics. **A.** Current-dependent increase in threshold for the first spike. **Ai)** The mean first spike threshold for all of the recorded excitatory cells was plotted as a function of the stimulus current intensities. (Linear fits for CG: $y = 0.084x - 50.98$, CA3: $y = 0.076x -$

54.59, hMC: $y = 0.089x - 56.93$, CA1: $y = 0.04x - 55.93$). Inset: At higher current injections, this increase in spike threshold saturates for the hMC. **Aii)** Same as in **Ai)** except for inhibitory interneurons. (Linear fits for PV: $y = -0.015x - 48.17$, SOM: $y = 0.0057x - 50.47$). **B.** Current dependence of the latency to first spike. Stronger current injections cause the cell to spike earlier. An exponential fit was used for both hMC (dashed grey curve, $y = 308.5 * e^{-x/276.1}$, adjusted $R^2 = 0.33$) and CA1 (dark yellow curve, $y = 1279.3 * e^{-x/44.2} - 25.6$, adjusted $R^2 = 0.93$). Given low correlation for the hMC, a linear fit was also used: red line, $y = -0.69x + 284.16$). **C.** Current dependency of the latency to first spike across other hippocampal neurons. **Ci)** Comparison across GC and CA3 pyramidal neurons. A linear fit was used to highlight the decrease in latency to first spike (GC: $y = -0.92x + 195.36$, CA3: $y = -0.14x + 123.9$). **Cii)** Same as **Ci)**, but for the inhibitory cells. (Linear fits: PV: $y = -0.49x + 111.76$, SOM: $y = -0.27x + 109.94$). For the SOM interneurons, only 1 cell (N=1) is shown for currents >140 pA. Colour scheme: GC (N= 9 cells): dark blue filled squares; CA3 (N = 8 cells): yellow triangles, CA1 (N = 7 cells): magenta pentagons; hMC (N= 14 cells): teal open circles; hilar PV (N = 8 cells): pink filled circles; hilar SOM (N = 9 cells): open cyan squares. The shaded area corresponds to the standard deviation.

Figure 5. Comparison of the spike threshold dynamics in various hippocampal neurons. Ai) Histogram of the first spike threshold in the presence of synaptic noise (black) and absence of synaptic noise (red) in hMCs. **Aii)** Cumulative function of the 1st spike threshold distribution across control (with synaptic noise, in black) and CNQX (without synaptic noise, in red) 1sts spike threshold values. **Aiii)** Mean 1st spike threshold values before and after the addition of CNQX (N = 14 cells). **Aiv)** The effects of MP fluctuations to the spike threshold in hMCs. Most cells with high spike threshold had low MP variance prior to the bath application of CNQX (i.e., only control values). Here each square represents the mean value for a given cell. Linear fit: $y = -0.24x - 40.0$. **Av)** Mean first spike threshold comparison across different hippocampal cell types. **B.** hMC exhibit a dynamic spike threshold. **Bi)** Example current-clamp response trace illustrating a difference in 9.6mV between the 1st and last evoked spike. **Bii)** Phase-plot of the hMC's response following a step-current injection. The arrow highlights the increase in spike threshold following successive spiking. **C.** Example responses from different cell types to a square pulse current injection in current-clamp mode: **Ci)** GC, **Cii)** CA3, **Ciii)** CA1, **Civ)** hilar PV and **Cv)** hilar SOM interneuron. The small arrow at the end of each trace denotes the increase in spike threshold between the first and last evoked spike. **D.** Comparison of the dynamic spike threshold across hippocampal cell types. CA3 pyramidal neurons were not shown here due to the low numbers of recorded spikes. For the hMC neurons, only 1 cell (N=1) had >10 spikes. Colour scheme: GC (N= 9 cells): dark blue filled squares; CA3 (N = 8 cells): yellow triangles, CA1 (N = 7 cells): magenta pentagons; hMC (N= 14 cells): teal open circles; hilar PV (N = 8 cells): pink filled circles; hilar SOM (N = 9 cells): open cyan squares. The shaded area denotes the standard deviation. n.s. = non-significant.

Figure 6. Spike threshold adaptation timescale. A. Example hMC response to the ramp current injection protocol. **Ai)** Two ramp currents (0) and (1) were injected with an interstimulus time interval t . The first stimulus (0) was always twice as strong (in amplitude) and twice as long (in duration) then the subsequent probe stimulus (1). **Aii)** In this example the stimulus ramp current was +500 pA and lasted 200 ms while the probe ramp current was +250 pA and lasted 100ms. The recovery from the spike threshold adaptation was measured by injecting the probe ramp current at different pre-selected times t (in this example, 50, 500, 1000ms). **Aiii)** Example hMC response to the stimulus ramp current injection in **Aii)**. **B.** Decay of the spike threshold adaptation in hMC. The difference in spike threshold between the first spike resulting from the first and second ramp current injection was plotted as a function of the interstimulus time t . The decay curve was fitted with an exponential ($y = 3.175e^{-x/570.42}$). The red open circles represent the average spike threshold, and the shaded area corresponds to the standard deviation. **C.** Example DG granule cell's response to the ramp current injection protocol. **Bi)** Same stimulation protocol as in **Ai)** except the stimulus amplitude is smaller. **Bii)** Example GC response to the stimulus ramp current injection (0), and various probe ramp current injections after $t = 50$ ms (1), $t = 500$ ms (2), $t = 1000$ ms (3). **D.** Same as in **6B**, except for DG granule cells. Due to absence of the spike threshold

adaptation, a linear fit was used instead of an exponential fit ($y = 0.0000139x - 0.287$) **E**. Comparison of the spike threshold adaptation in hippocampal neurons. **Ei**) For CA3 pyramidal neurons. **Eii**) For CA1 pyramidal neurons. **Eiii**) For PV interneurons. **Eiv**) For SOM interneurons. In panels **6B**, **6D** and **6E**, we show all the sampled points (small, filled dots) for each cell type and each RAMP delay, together with their averages (open symbols) and their standard deviation (shaded region). **F**. Comparison of the decay of the spike threshold adaptation. **Fi**) For all the excitatory neuron subtypes. An exponential fit was also used for the CA3 ($y = 4.031e^{-x/462.58}$) and for the CA1 neurons ($y = 1.0432e^{-x/189.4}$) **Fii**) For all hilar interneuron subtypes. An exponential fit was also used for the hilar PV ($y = 1.521e^{-x/157.76}$) and for the hilar SOM ($y = 1.326e^{-x/344.76}$) neuron. Colour scheme: GC (N= 9 cells): dark blue filled squares; CA3 (N = 8 cells): yellow triangles, CA1 (N = 7 cells): magenta pentagons; hMC (N= 14 cells): teal open circles; hilar PV (N = 8 cells): pink filled circles; hilar SOM (N = 9 cells): open cyan squares.

Figure 7. Model simulation. **A**. Representative spikes for three different step current intensities. This protocol is used to probe for the model properties in all the other panels (except for the threshold decay in panel **E**, where the ramp input protocol is used as explained in Fig. 5). Dashed lines are guides to help identify the increase of the threshold and AHP depth. **B**. The input-dependent threshold follows closely the sigmoidal trend observed experimentally. **C**. The latency to first spike tends to diverge for small inputs similarly in model and experiments. **D**. Spike-dependent threshold increase; the experimental data (circles) are the same as presented in Fig. 3C for hMCs. The side-pointing empty triangles are the experimental data averaged over high (190 to 300 pA) and low (70 to 180 pA) input currents. The model threshold increase was averaged over input current intensity (squares) ranging from 70 to 350 pA. Up-(down-)pointing triangles show the behaviour of the model for high (low) injected current. **E**. The decay has a similar time constant and follows closely the one from hMCs. **F**. Covariance of the AHP minimum potential with the spike threshold, supporting the linear reset rule implemented in the model. The slope of the covariance remains constant at 0.8 for a wide range of inputs (inset) in both experiments and model (hence the chosen α in Table 2). All shaded areas are standard deviation except for panel **F** inset, where it represents the 95% confidence interval from the best fitting slope of the covariance.

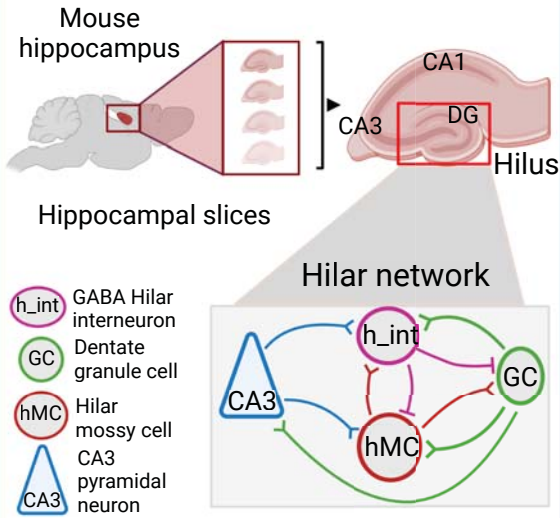
Figure 8. Robustness of the model with respect to threshold parameters. **A**. Threshold as a function of the injected current (same legend as in panel C). **B**. Threshold increase as a function of the spike number. **C**. Latency as a function of the injected current. **D**. Threshold decay as a function of the delay after the initial ramp stimulus. The default configuration of parameters is given in Table 2 and shown in Fig. 6. The hMC data are the same as in Fig. 6B. The other configurations have the altered parameters given in the legends. The same symbol and colour are used for each unique configuration across all panels. Shaded area is the standard deviation. The model is robust to variations in certain parameters, although choosing the best fit for one of the features may interfere with the fit performance of other features, suggesting a covariance between hMCs membrane parameters. The threshold-AHP minimum covariance plot is not affected by any of these parameters.

Abstract figure.

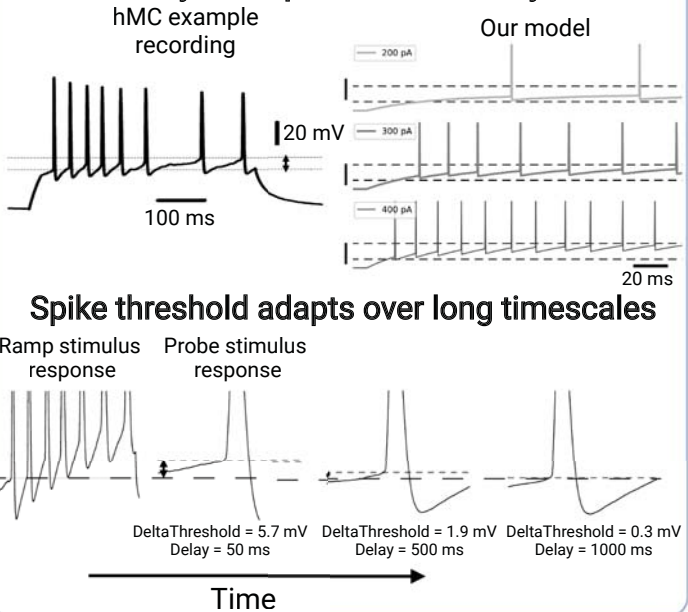
In the hilar network, a micro-circuit in the dentate gyrus (DG), the hilar mossy cells (hMCs) are the main excitatory feedback input to DG. Although the hMCs exhibit sparse spiking *in vivo*, it is not known whether this is a consequence of their intrinsic biophysics or the hilar inhibitory interneurons. To test the contribution of hMC intrinsic properties, we performed whole-cell patch recordings of the hMCs and other main cell types in the mouse hilar network. All tested neurons exhibited an increase in the threshold voltage following successive spiking and their spike threshold were dependent on the stimulus intensity – a new finding. Further, only the CA3 and hMC exhibited a slow adaptation lasting over hundreds of

milliseconds to this increase in spike threshold. We developed a new integrate-and-fire-like model that captured the threshold dynamics of hMCs. This might pave the way for future network simulations, shedding light on memory dynamics. Created with BioRender.com

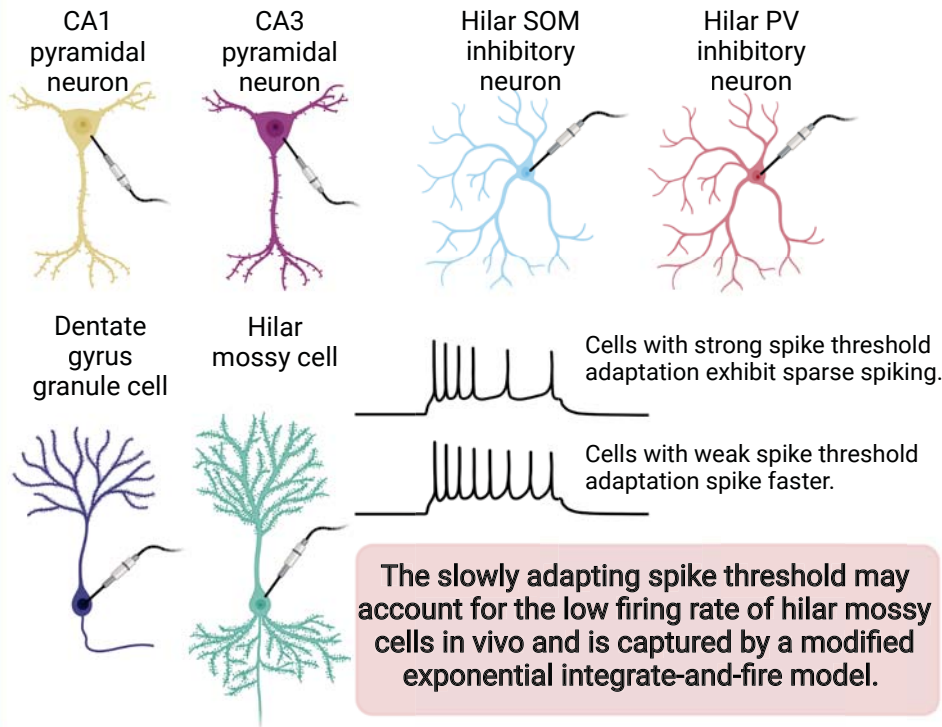
In vitro recordings of hippocampal slices



Hilar mossy cell spike threshold dynamics

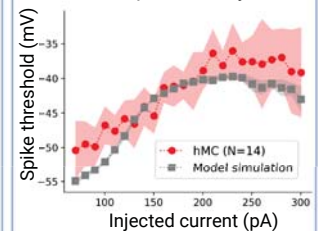


Electrophysiological characterization

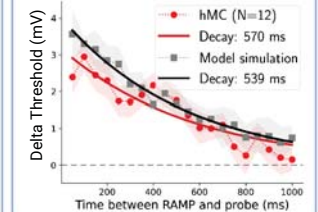


Hilar Mossy cell vs model

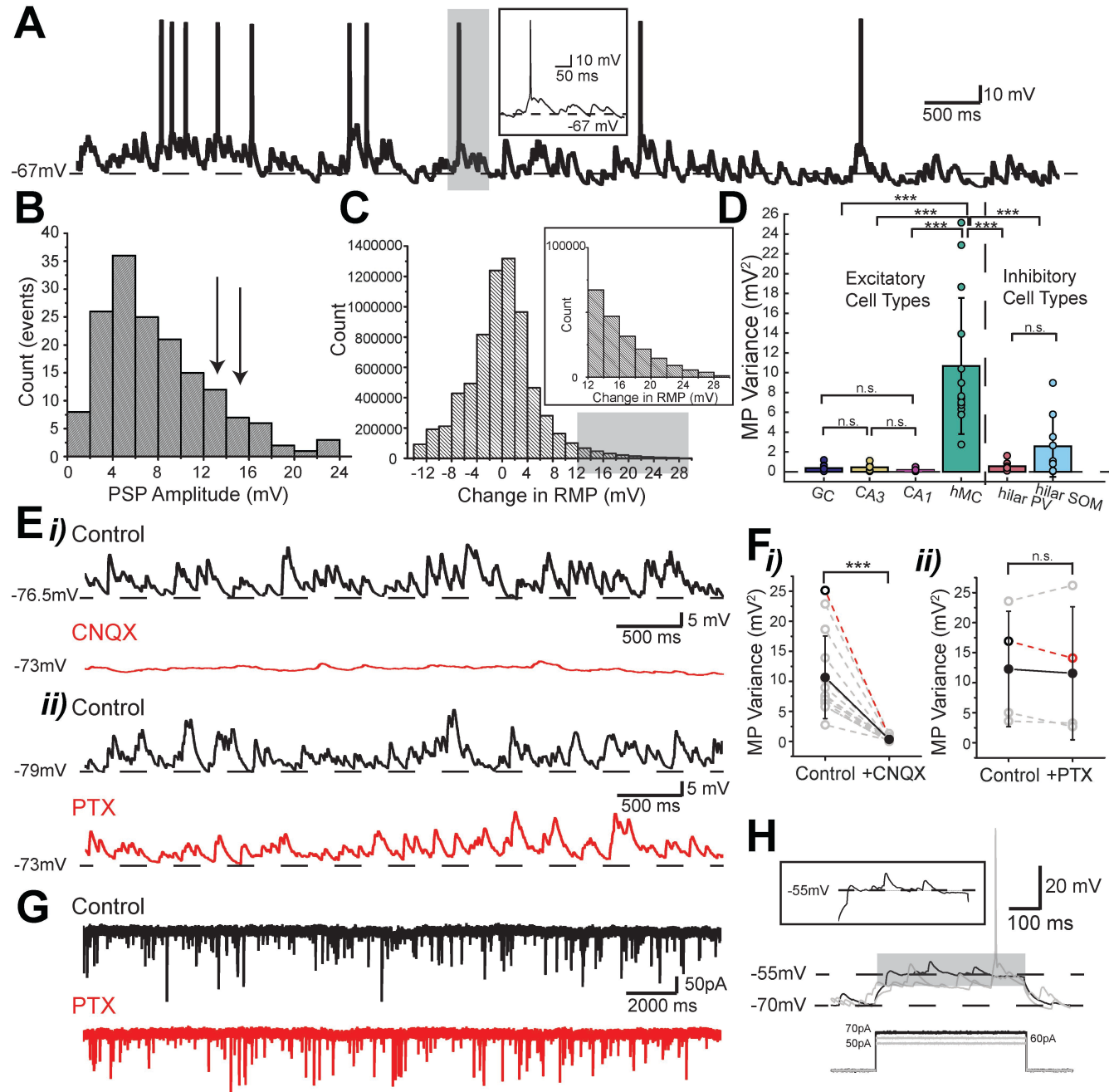
The threshold increases coupled both to current and spike activity...

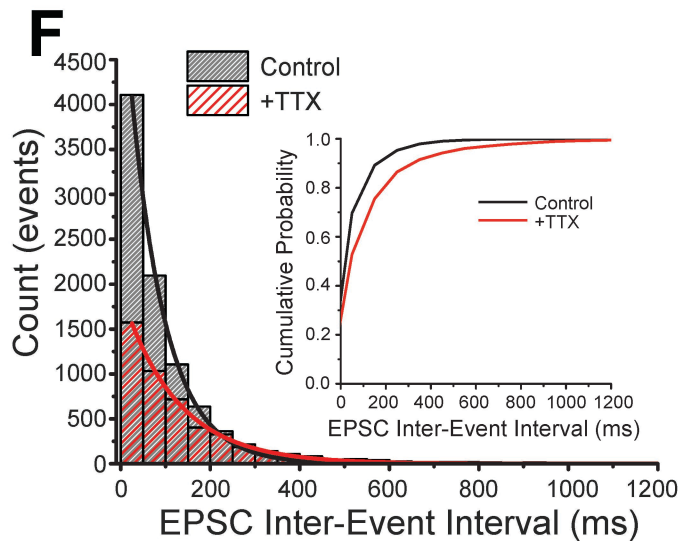
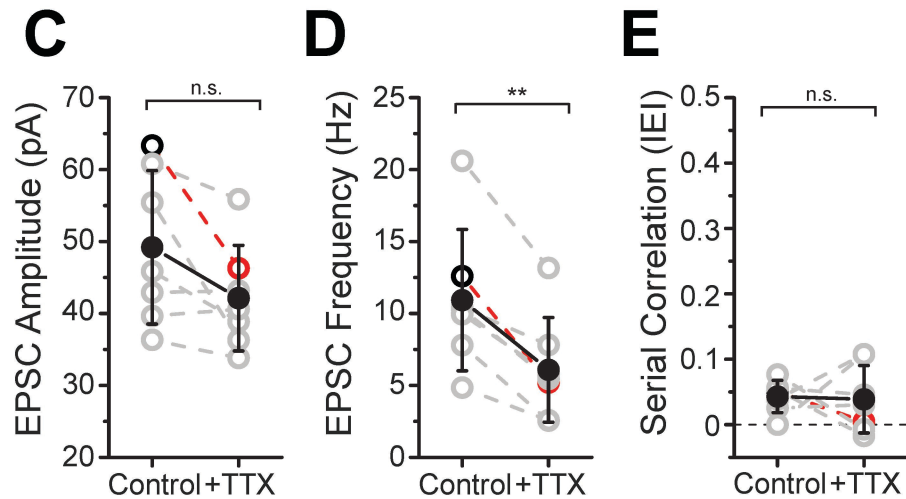
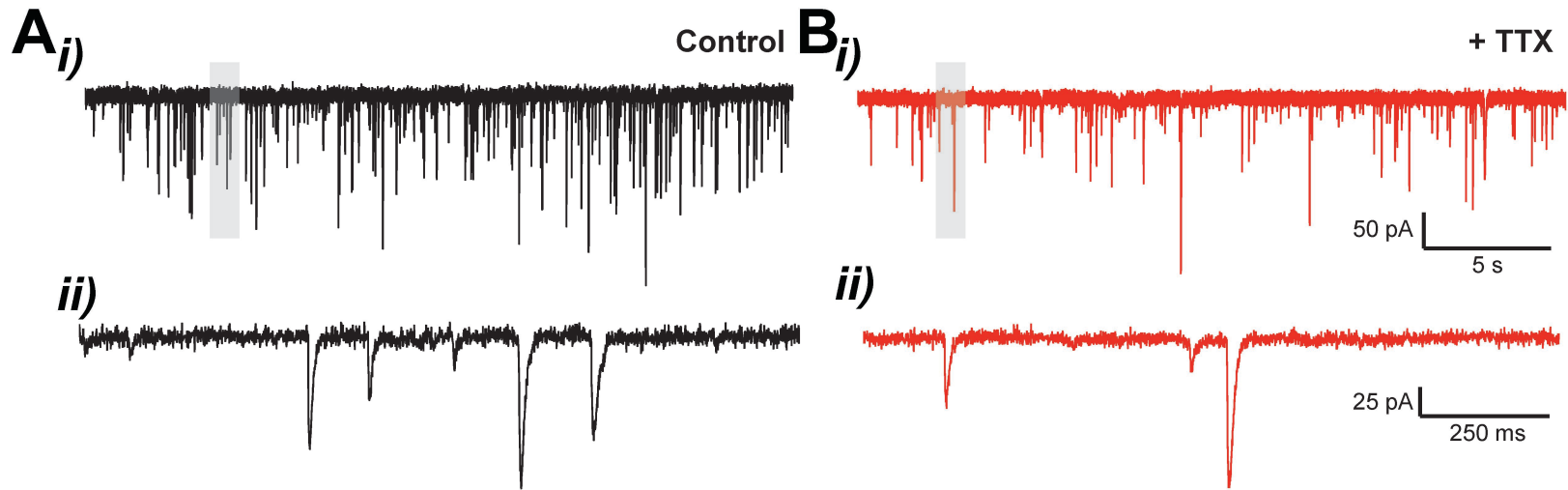


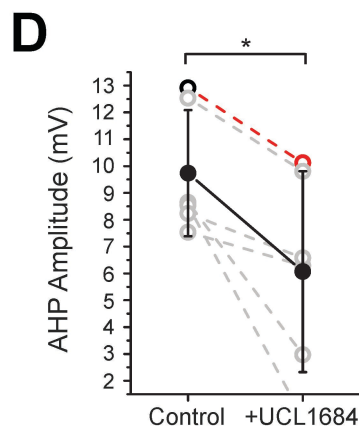
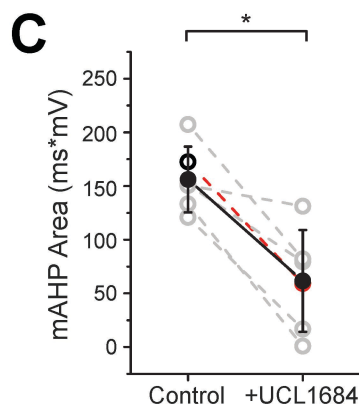
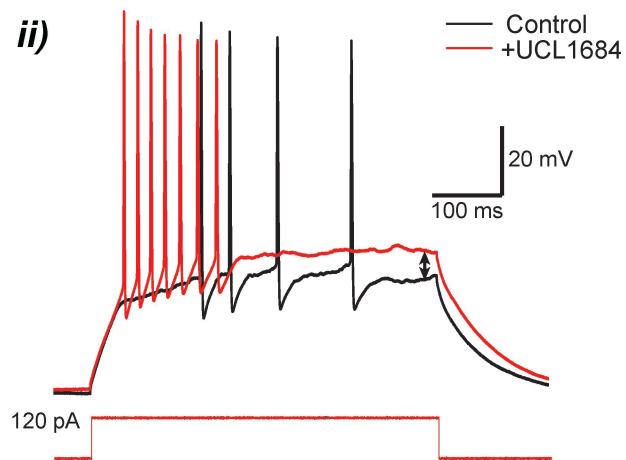
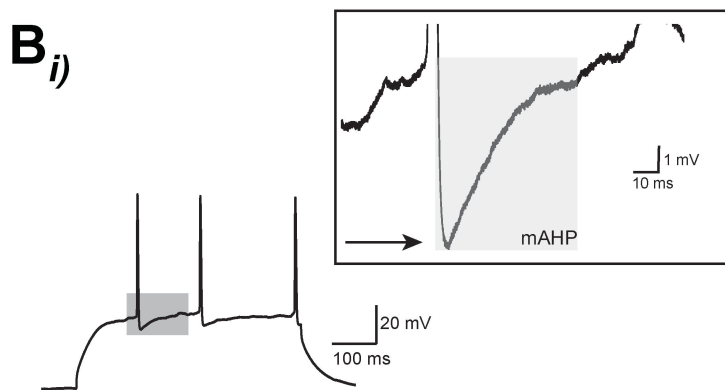
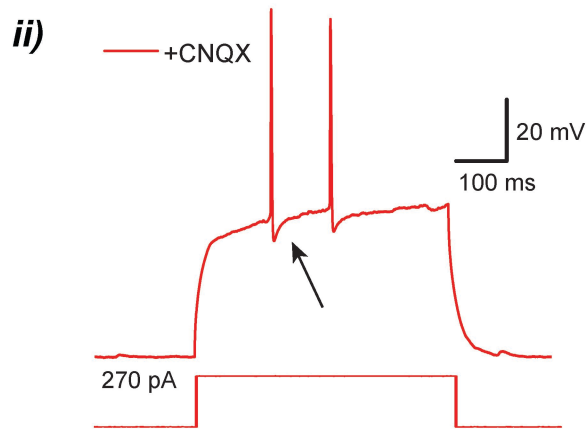
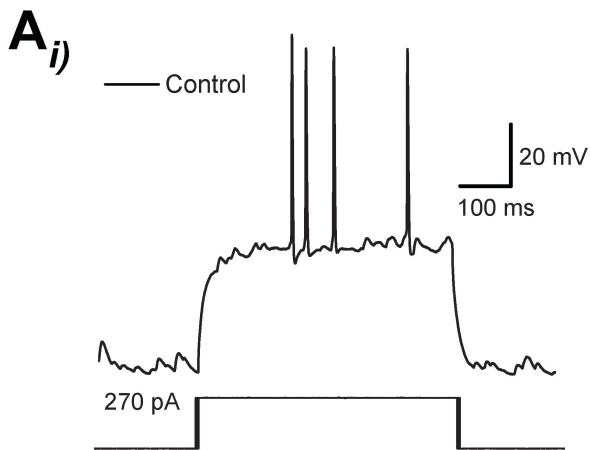
... and decays over long times

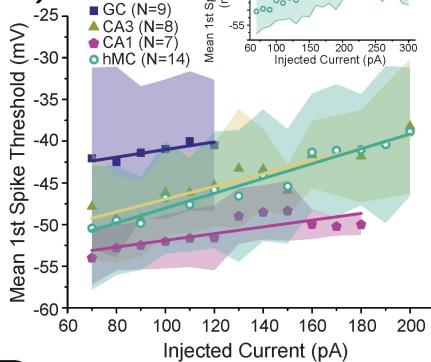
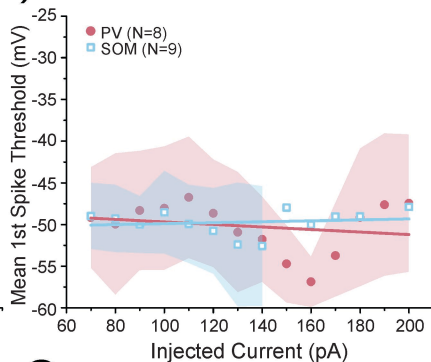
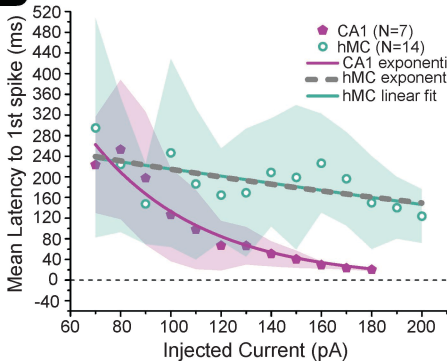
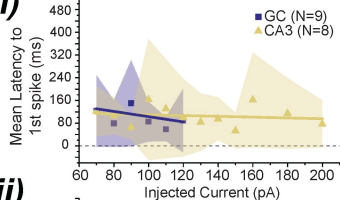


The Journal of
Physiology







A**ii)****B****C****ii)**